Quaternary Science Reviews 222 (2019) 105875

Contents lists available at ScienceDirect

Quaternary Science Reviews

journal homepage: www.elsevier.com/locate/quascirev

Chronology and sedimentology of a new 2.9 ka annually laminated record from South Sawtooth Lake, Ellesmere Island

Francois Lapointe [a, b, *], Pierre Francus [b, c], Joseph S. Stoner [d], Mark B. Abbott [e], Nicholas L. Balascio [f], Timothty L. Cook [a], Raymond S. Bradley [a], Steven L. Forman [g], Mark Besonen [h], Guillaume St-Onge [c, i]

[a] Climate Science Center, Department of Geosciences, University of Massachusetts, Amherst, MA 01003, USA
[b] Centre - Eau Terre Environnement, Institut National de la Recherche Scientifique, Canada Research Chair in Environmental Sedimentology, Québec, G1K 9A9, Canada
[c] GEOTOP, Université du Québec à Montréal, Québec, Montreal, H3C 3P8, Canada
[d] College of Earth, Ocean, and Atmospheric Sciences, Oregon State University, Corvallis, OR 97331, USA
[e] Department of Geology and Planetary Science, University of Pittsburgh, Pittsburgh, PA 15260, USA
[f] Department of Geology, College William and Mary, 251 Jamestown Road, Williamsburg VA 23187 USA
[g] Department of Geology, Baylor University, College of Arts and Sciences, One Bear Place #97354, Waco, TX 76798, USA
[h] Harte Research Institute for Gulf of Mexico Studies, Texas A&M University - Corpus Christi, Corpus Christi, TX 78412, USA
[i] Institut des Sciences de la mer de Rimouski, Canada Research Chair in Marine Geology, Université du Québec à Rimouski, 310 allée des Ursulines, Rimouski, Québec, G5L 3A1, Canada

ARTICLE INFO

Article history:
Received 24 April 2019
Received in revised form
9 August 2019
Accepted 9 August 2019
Available online 17 September 2019

Keywords:
Holocene
Arctic climate
Varves
Paleoclimatology
Chronology
Paleomagnetism

ABSTRACT

Few annually laminated (varved) lacustrine records exist in the Arctic, but these high-resolution climate archives are needed to better understand abrupt climate change and the natural mode of climate variability of this sensitive region. This paper presents a new high-resolution 2900-year long varved lake sediment record from the Fosheim Peninsula, Ellesmere Island. The varve chronology is based on multiple varve counts made on high-resolution scanning electron microscope images of overlapping sediment thin sections, and is supported by several independent dating techniques, including ^{137}Cs and ^{210}Pb analysis, one optically stimulated luminescence age located close to the bottom of the composite sequence, and comparison between paleomagnetic variations of this record and the longest High-Arctic varve record, Lower Murray Lake, which confirms the reliability of the Sawtooth chronology. High-resolution backscattered images examined under a scanning electron microscope (SEM) were crucial to giving a more detailed view of sedimentation processes in the lake and thus help to delineate varves more precisely than in conventional image analysis. Fine-scale geochemical analysis reveals that lake sedimentation is mainly clastic and that elemental geochemistry is influenced by grain-size. Principal component analysis of multiple proxies and the coarse grain-size fraction of South Sawtooth Lake display similar fluctuations to the nearby Agassiz Ice Cap ∂^{18}O record, including lower values during the Little Ice Age cold period. These results show this new high-resolution and continuous record has a reliable varve chronology and is sensitive to temperature variability. South Sawtooth Lake's mean sedimentation rate of 1.67 mm a^{-1} is higher than any other sedimentary sequence in the High Arctic providing a unique opportunity for extracting new, high-resolution paleoclimatological and paleoenvironmental record in a region where few other records currently exist.

1. Introduction

The Arctic has undergone substantial warming during the last decade. This trend is expected to increase with further loss of sea-ice and increased glacier melt, thus accelerating the related positive feedback processes. Due to limited instrumental data from the

* Corresponding author. Climate Science Center, Department of Geosciences, University of Massachusetts, Amherst, MA 01003, USA.
E-mail address: flapointe@umass.edu (F. Lapointe).

https://doi.org/10.1016/j.quascirev.2019.105875
0277-3791/

region, there is still a huge lack of understanding of the Arctic climate system (Cohen et al., 2014). High-resolution climate records can provide meaningful information about past temperature and precipitation (e.g. Lapointe et al., 2017). However, published climate archives from the region are insufficient and their spatial distribution is limited in extent. Development of reliable paleoclimate records from the High Arctic is especially challenging given the limited success of radiocarbon dating as a means of constraining the chronology of lacustrine records from Artic lakes. This is largely caused by limited biological productivity and the presence of aged carbon stored in watersheds which often leads to unreliable age determinations (Abbott and Stafford, 1996). In contrast, the precision and accuracy of varve-count chronologies can provide superior chronologies compared to those based purely on radiometric methods (Zolitschka et al., 2015). Yet new annually laminated records from the Canadian Arctic must be tested against other independent dating methods to demonstrate that they are indeed varves. This paper provides a new varved record from South Sawtooth Lake, Ellesmere Island (hereafter, SSL). The varve chronology is supported by several independent dating techniques, including radiometric analysis of the recent record, optically stimulated luminescence dating (OSL), and paleomagnetic variations over the past 2900 years. This paper is an extension of previous work undertaken at SSL (Francus et al., 2002) using new sediment cores to establish a chronology and characterize the stratigraphy. We then extract physical and geochemical properties of the sediment in order to establish a basis for further paleoclimatic investigations using this record.

1.1. Study site

SSL (79° 20′N, 83°51′W, 280 m a.s.l.) is located on the Fosheim peninsula in the Eastern Canadian High-Arctic (Fig. 1). This site has been the focus of several studies (Francus et al., 2002, 2008; Perren et al., 2003; Lewis et al., 2005), which indicate that sediments in the lake are varved. The surficial geology of the area is composed of blanket and veneer tills. Deglaciation started around 5800 BCE (7800 B.P.) with present-day conditions reached around 4300 BCE (6300 B.P.) (England, 1983). The bedrock geology of the SSL watershed is composed mainly of Triassic sandstones and

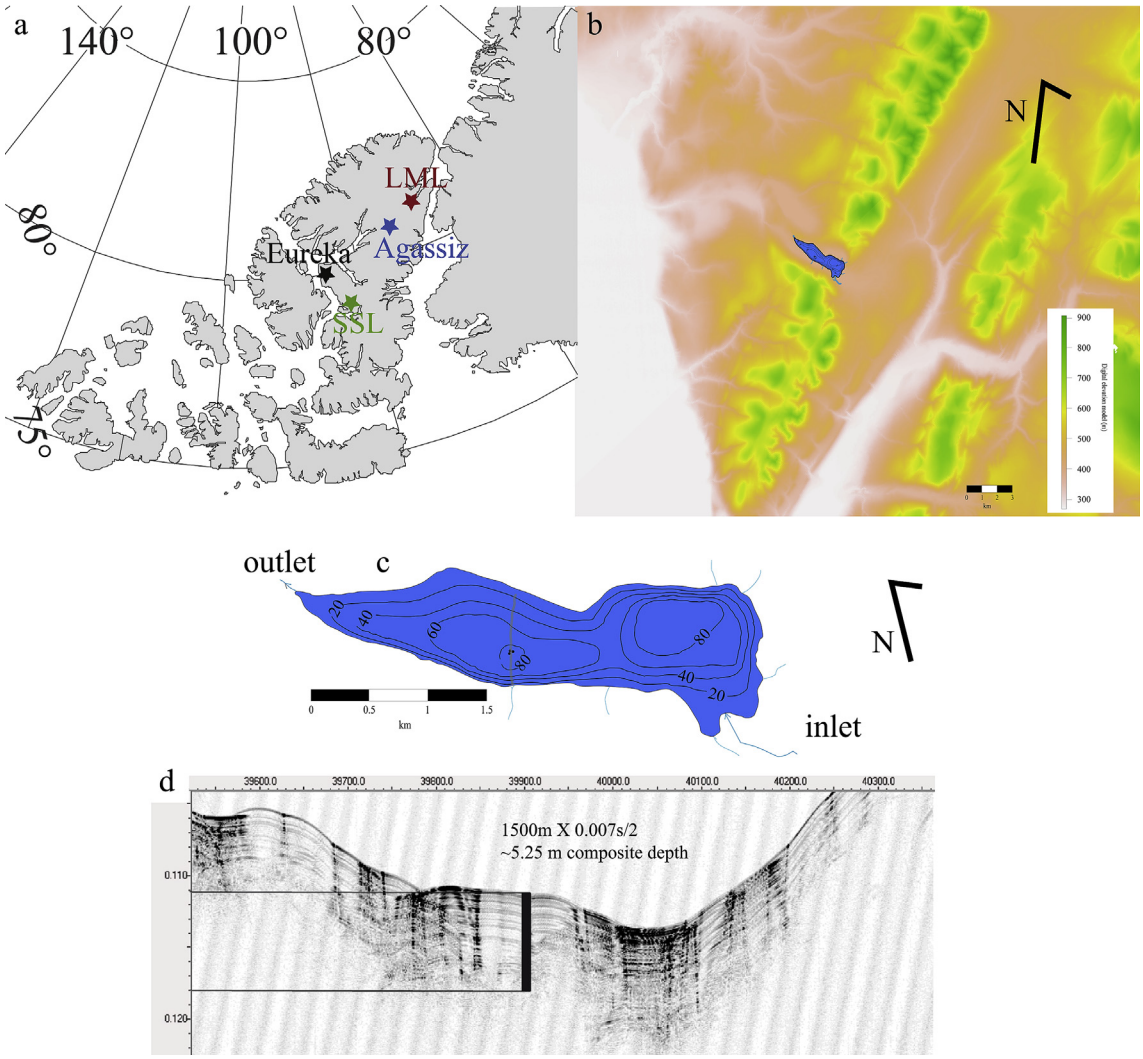

Fig. 1. a) Location of South Sawtooth Lake in the Canadian Arctic, Ellesmere Island. Green, red, blue and black stars denote South Sawtooth Lake (SSL) Lower Murray Lake (LML), Agassiz Ice Cap and Eureka weather station, respectively. b) Land digital elevation model (DEM) base map from the ArcticDEM 7 Polar Geoscience Center showing SSL in the Sawtooth Range. Map created in R. c) SSL bathymetry showing SS12-12, the location of the composite sequence (black circles). The gray line crossing the lake corresponds to the seismic profile in d. d) SEG-Y data from the seismic profile were processed using the *Kingdom Suite*®. Subbottom data were collected in the lake using a Edge Tech 3100 Chirp at a frequency 4–24 kHz. (For interpretation of the references to colour in this figure legend, the reader is referred to the Web version of this article.)

calcareous siltstones, with minor concentrations of limestone and shale (Geological Survey of Canada, 1972). The lake and its watershed surface area are ~2.6 km^2 and 47 km^2, respectively, with a maximum elevation of ~915 m a.s.l. A single tributary spills into the lake from the southeast, while the outlet is situated at the northwestern end (Francus et al., 2008). SSL is an elongated lake divided into a proximal and a distal basin (100 and 82 m deep, respectively) separated by a 60-m deep sill. This configuration limits erosion in the distal basin, where the sediment cores were recovered (e.g. Francus et al., 2008). A seismic survey was conducted in 2006 revealing that the distal basin is devoid of major mass movement deposits (Fig. 1b and c), and thus well suited for paleoclimatological investigations.

The geomorphic setting of the study area with its surrounding mountains and highlands limit the incursion of cold Arctic Ocean air masses and cyclonic activity from Baffin Bay (Edlund and Alt, 1989). From 1948 to 2016, the average monthly temperature at Eureka (the nearest weather station, 84 km to the NW and 10m asl), were 2.5, 5.9, and 3.3 °C during June, July and August, respectively. Described as an extreme polar desert, the region's annual precipitation is 65 mm and ~25 mm falls as rain according to the Eureka weather station. However, a temporary weather station at SSL recorded twice the amount of rain recorded at Eureka (Lewis et al., 2005). Precipitation for June and July of 1994 at a nearby site in the Sawtooth Range reached 64 mm, similar to the mean annual value at Eureka (Lewkowicz and Hartshorn, 1998). It is also worth mentioning that great amounts of rain were witnessed during the field season of 2012 at SSL in the end of May, although no rain was recorded at Eureka during that time. Thus, the orographic influence on climate combined with the steep slopes with elevation reaching ~915 m asl (Fig. 1b) promote hillslope processes and sediment transfer into the lake, resulting in SSL having one of the highest sedimentation rates in the region (Francus et al., 2008).

The annual couplets result from seasonal differences in the lake. Clay caps are formed by the settling of fine clay particles during the winter when the lake is ice-covered (2–3 m thick ice) and the turbulence in the water column is low to absent. In turn, deposition of coarser sediments associated with overflows triggered by early snow melt and occasional rainfall events occurs later in the summer season (Francus et al., 2008).

2. Methods

2.1. Chronology

2.1.1. Cores, thin sections and imageries

Overlapping core sections were recovered from three holes drilled in the lake-ice surface at the deepest water depth location (82 m) in June 2012. A total of 15 core sections were retrieved using a UWITEC percussion corer equipped with a locking piston allowing for multiple drives to be recovered from each hole. Cores were first analyzed using a Siemens SOMATOM Definition AS+ 128 CT-Scanner at INRS in Québec City in order to establish the composite sequence. The upper 4.98 m contains finely laminated sediments, which is the focus of this analysis. A total of 35 metal trays (each 19 cm long), filled with sediment removed from the cores (Francus and Asikainen, 2001), were first flash frozen by slow immersion in liquid nitrogen and then subsequently freeze dried (Normandeau et al., 2019). These 19 cm-long sediment profiles were collected in order to have a 1 cm overlap between them.

Dried sediment in the trays was then impregnated with epoxy resin (Lamoureux, 1994) and 100 overlapping thin sections were made to cover the laminated interval. Thin sections (sediment exposed ~5 × 2 cm) were digitized using a flatbed scanner at 2400 dpi (1 pixel = 10.6 μm). Using the image analysis software package developed at INRS (Francus and Nobert, 2007), regions of interest (ROIs) were identified on the digital images. ROIs were labeled with three character alphabetic codes such as “aag” (see Fig. 2b and c for an example). A Zeiss Evo® 50 scanning electron microscope (SEM) was then used to acquire ~8000 images in backscattered mode following the methods of Lapointe et al. (2012). These high-resolution images were used to count varves as they provide superior contrast relative to optical images and because many laminae are less than 0.5 mm and hard to delineate using digital flatbed scan images, or other common techniques.

2.1.2. Radiometric dating

The uppermost part (18.25 cm) of a gravity core (undisturbed sediment) were extruded in the field and measured continuously at a 1 cm increment for radionuclides (^{210}Pb, ^{137}Cs) at the University of Pittsburgh. ^{210}Pb and ^{137}Cs activities were measured using a Canberra Gamma Spectrometer. The chronology was established using the constant rate of supply (CRS) model (Appleby, 2002).

2.1.3. Paleomagnetic variations

Paleomagnetic secular variations were derived from U-channel samples that were analyzed through progressive alternating field (AF) demagnetization measured at 1 cm intervals, using a 2G EnterprisesTM model 755–1.65UC superconducting rock magnetometer at the Oregon State University's Paleo- and Environmental Magnetism Laboratory. The natural remanent magnetization (NRM) was measured and progressively demagnetized using stepwise AF up to 70 mT in 5 mT steps to isolate the characteristic remanent magnetization (ChRM) and collect the inclination of the ChRM. U-channel results were processed using the UPmag software (Xuan and Channell, 2009).

2.1.4. Optically stimulated luminescence dating

Optically stimulated luminescence (OSL) dating provides a measure of time since sediment grains were deposited and shielded from further light exposure, which often effectively resets the luminescence signal to a low defineable level (Murray and Olley, 2002). A time-dependent luminescence signal is acquired upon buried with exposure to ionizing radiation (α, β and γ) from the decay of radioisotopes in the surrounding sediments. This exposure to ionizing radiation and to a lesser extent, to cosmic radiation, results in displaced electrons within the quartz crystal lattice, with a proportion of this acquired charge increasing with time, named as a luminescence emission.

Single aliquot regeneration (SAR) protocols (Murray and Wintle, 2003; Olley et al., 2004; Wintle and Murray, 2006) were used in this study to estimate the apparent equivalent dose of the 44-20 μm quartz fraction for 58 to 86 separate aliquots (Table 1). Each aliquot contained approximately 100–500 quartz grains corresponding to a 1 mm circular diameter of grains adhered (with silicon) to a 1 cm diameter circular aluminum disc. This aliquot size was chosen to maximize light output for the natural emissions with excitation; smaller aliquots often yielded insufficient emissions (<400 photon counts s^{-1}).

The quartz fraction was isolated by density separations using the heavy liquid Na–polytungstate, and a 40-min immersion in HF (40%) was applied to etch the outer ~10 μm of grains, which is affected by alpha radiation (Mejdahl and Christiansen, 1994). Finally, quartz grains were rinsed in HCl (10%) to remove any insoluble fluorides. The purity of quartz separates was evaluated by petrographic inspection, point counting of a representative aliquot, and was tested by exposing aliquots to infrared excitation (1.08 W from a laser diode at 845 ± 4 nm), which preferentially excites feldspar minerals. Samples measured showed weak emissions (<200 counts/second), at or close to background counts with

infrared excitation, and ratio of emissions from blue to infrared excitation of >20, indicating a spectrally pure quartz extract (Duller, 2003).

An automated Risø TL/OSL–DA–15 system (Bøtter-Jensen et al., 2000) was used for SAR analyses. Blue light excitation (470 ± 20 nm) was from an array of 30 light-emitting diodes that

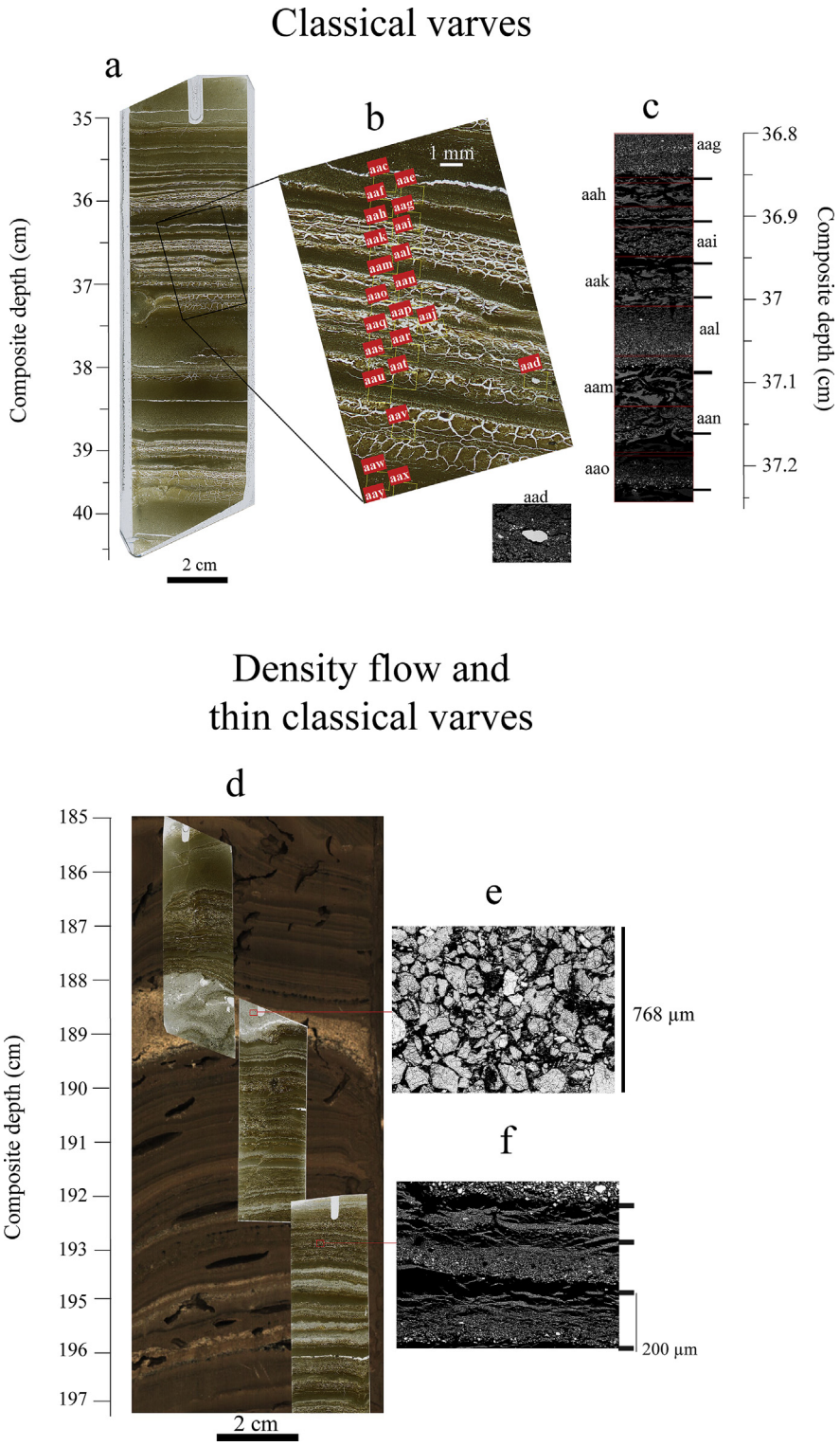

Fig. 2. a) Flat-bed scan of thin section SS12-12-2-1s-C1. b) Enlargement of the black rectangle with Regions of interest (ROIs) aac to aay. C) ROIs aag to aao acquired at the scanning electron microscope are identified on the thin section, red rectangles are selected ROIs (aag to aao). Black lines indicate varve boundaries. d) Section of ss12-12-2-2P showing coarse grain-size (e) and thin varves (f). High-resolution SEM imageries enhance the ability to define varve boundaries. Black rectangles at the right of the SEM image represent the varve boundaries. Note that the sand lamina presented in panel e is a density flow. (For interpretation of the references to colour in this figure legend, the reader is referred to the Web version of this article.)

Table 1
Optically Stimulated Luminescence (OSL) ages[a] on quartz from South Sawtooth Lake, Ellesmere Island.

Core/depth	Lab number	Aliquots[b]	Grain-size (μm)	Equivalent dose (Gray)[c]	Over-dispersion (%)[d]	U (ppm)[e]	Th (ppm)[e]	K (%)	H2O (%)	Cosmic dose rate m Gray a^{-1}[f]	Dose rate m Gray a^{-1}	OSL age (a^{-1})[g]
SS12-10-1-3P 0−4 cm	BG4055	78/94	20−44	3.21 ± 0.34	100 ± 8	3.51 ± 0.01	13.05 ± 0.01	2.61 ± 0.01	35 ± 5	0.05 ± 0.005	3.31 ± 0.17	960 ± 120
SS12-10-1-3P 150−154 cm	BG4057	86/99	20−44	3.94 ± 0.42	116 ± 20	3.43 ± 0.01	13.3 ± 0.01	2.23 ± 0.01	35 ± 5	0.03 ± 0.003	3.03 ± 0.15	1290 ± 165
SS12-10-1-3P 174−178 cm	BG4058	84/112	20−44	8.84 ± 0.98	72 ± 20	3.20 ± 0.01	12.1¿ 0.01	2.69 ± 0.01	35 ± 5	0.03 ± 0.003	3.25 ± 0.16	2720 ± 355
SS12-12-2-3P 174−178 cm	BG4056	56/68	20−44	27.62 ± 0.95	22 ± 2	3.22 ± 0.01	13.5 ± 0.01	3.09 ± 0.01	35 ± 5	0.03 ± 0.03	3.62 ± 0.18	7630 ± 595

[a] OSL dates are referenced to 2010 BCE.
[b] Aliquots used in equivalent dose calculations versus original aliquots measured.
[c] Equivalent dose calculated on a pure quartz fraction with about 40−100 grains/aliquot and analyzed under blue-light excitation (470 ± 29 nm) by single aliquot regeneration protocols (Murray and Wintle, 2003). The central age model of Galbraith et al. (1999) was used to calculate equivalent dose when overdispersion values are <25% (at one sigma errors; a finite mixture model was used with overdispersion with values > 25% to determine the youngest equivalent dose population.
[d] Values reflect precision beyond instrumental errors; values ≤ 25% (at 1 sigma limit) indicate low dispersion in equivalent dose values and an unimodal distribution.
[e] U, Th and K content analyzed by inductively-coupled plasma-mass spectrometry analyzed by ALS Laboratories, Reno, NV; U content includes Rb equivalent.
[f] Cosmic dose rate calculated from parameters in Prescott and Hutton (1994).
[g] Systematic and random errors calculated in a quadrature at one standard deviation. Datum is 2010 CE.

deliver ~15 mW cm^{-2} to the sample position at 90% power. Optical stimulation for all samples was completed at an elevated temperature (125 °C) using a heating rate of 5 °C s^{-1}.

The U and Th content of the sediments, assuming secular equilibrium in the decay series and ^{4}K, were determined by inductively coupled plasma-mass spectrometry (ICP-MS) analyzed by ALS Laboratories, Reno, NV. The beta and gamma doses were adjusted according to grain diameter to compensate for mass attenuation (Fain et al., 1999). A significant cosmic ray component between 0.03 and 0.05 mGy a^{-1} was included in the estimated dose rate taking into account the current depth of burial (Prescott and Hutton, 1994). A moisture content (by weight) of 35 ± 5% was used in dose rate calculations, which reflects the variability in current field moisture conditions. More information about OSL can be found in the Supplementary data.

2.2. Annual grain-size data

The 8-bit gray-scale SEM images (1024 × 768 pixels) collected from thin sections were transformed into black and white to obtain particle measurements for each year of sedimentation (Francus and Pirard, 2004). For this study, several grain-size indices were measured including the median, 90th, and 99th percentile diameters (D50, D90 and D99, respectively), the standard deviation (SD), the maximum diameter ($MaxD_0$) and the weight % of the following fractions: <16 μm, <20 μm, <30 μm, 16−33 μm, 33−69 μm and >69 μm. Weight was calculated using the formula: $((4/3)*\pi*((D_0/2)^3))*2.65$ with D_0 being the apparent disk diameter (Francus et al., 2002).

2.3. μ-XRF analysis

An ITRAX core scanner, available at INRS-ETE in Québec City, was used to measure high-resolution geochemical variations (Croudace et al., 2006) using a molybdenum tube. The data acquisition was performed with a 100 μm resolution and an exposure time of 15s. Voltage and current were 30 kV and 30 mA, respectively with count per second (cps) values ranging from 26,000−34,000. A dispersive energy spectrum is acquired for each measurement point and peak are integrals calculated for each element. All elements were normalized by the total number of counts for each spectrum expressed in thousands.

2.4. Density proxies

Tomodensitometric 3D images correspond to the 3D X-ray attenuation of the objects in the sample, where higher attenuations represent higher densities and higher atomic numbers (Duliu, 1999). Cores were scanned with X-ray peak energy of 140 kV with 250 mA current. Tomograms measuring 512 X 512 pixels were acquired continuously at every 0.4 mm, along a 0.6 mm-thick slice resulting in an overlap of 0.2 mm between each tomogram. The open source ImageJ package was used to reconstruct longitudinal profiles from tomograms using the DICOM format. Gray-level values from these DICOM folders correspond to the attenuation values expressed in Houndsfield Units (HU), a proxy for relative density (Duchesne et al., 2009; Fortin et al., 2013).

2.5. Statistical analysis

Principal components analysis (PCA) was performed on the multiproxy dataset using « FactoMineR (v1.33) » package (Husson et al., 2016) of the software R (R Team Development, 2008). Prior to the PCA, all proxy data were normalized.

3. Results and interpretations

3.1. Sedimentary facies and varve counting criteria

Varves found at SSL are mainly clastic, and six main facies were previously described (Francus et al., 2008). The most common lithofacies is composed of a fine silt layer deposited by nival melt runoff that is overlain by a clay cap. The clay caps, which are composed of clay-sized particles, and deposited during the 8−10 months of winter ice cover. These can be observed in backscattered SEM imageries as uniform light gray areas (Fig. 2c,f). As described in Francus et al. (2008), clay caps are typically distinguishable by wavy horizontal cracks formed when the sediments are freeze-dried during preparation of thin-sections. The clays caps represent the main feature used to delineate varves at SSL. Some density flow (sand laminae) deposits have also been observed (Fig. 2e), but there are only 38 of these units over a 2900-long varved sequence. Althought the density flow facies can be triggered by rapidly deposited mass movement events, it can not be ruled out that they are the consequence of large rainfall events, thus climatologically-induced (Francus et al., 2008; Lapointe et al., 2012). Therefore,

those layers are included in the chronology. Density flows are composed of a mixture of sediment and water in which the volume and mass of sediment exceeds that of water (Major, 2003). Thicker graded beds (Fig. 3e; turbidites) were also observed in the sequence and these are also different than the regular pattern of sedimentation. The base of a turbidite is typically poorly sorted and coarse grained as it is the result of an energetic turbiditic flow, in which finer particles are deposited after the coarse layer base as the flow wanes and further deposition occurs through sediment settling (Mulder and Alexander, 2001). These beds have a median size of 2.3 mm (maximum: 51 mm). In rare instances (only 26 occurrences in the 2900 year sequence), dropstones or isolated grains can be found (Fig. 2; ROI: aad), and they are typically located within the upper part of the graded beds or within the clay caps themselves (e.g. Fig. 2; ROI aad). These isolated grains were not integrated in the grain-size analysis.

Less than 2% of the varve intervals were not as easy to delineate (e.g. Fig. 3b). Analysis of these diffuse intervals relied on the superior contrast of SEM images compared to the thin section photographs (Fig. 3c). For example, red horizontal rectangles depict varve boundaries using the thin section photographs alone, while the black horizontal lines delimit varves based on inspection of the higher definition SEM images (Fig. 3c). As mentioned above, clay caps are typically distinguishable by wavy cracks when looking at thin section optical images. However, in conjunction with the presence of cracks (i.e. Fig. 2f), there are a few wavy varves (<25 over the past 2900 years) where silt sized detrital input can be detected as well (Fig. 3d, S1). These are unlikely to have been

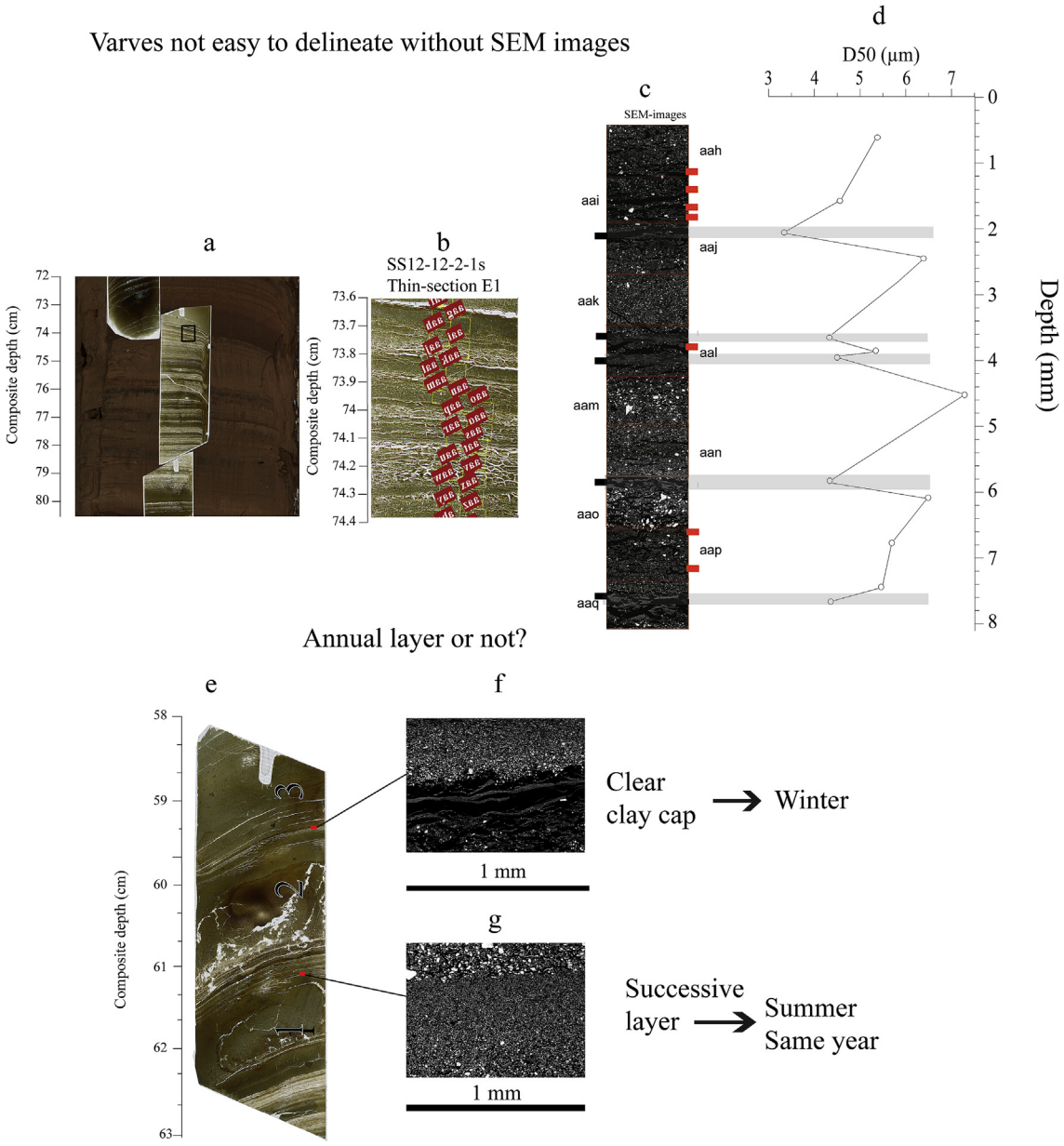

Fig. 3. a) Same as Fig. 2, but with thin section ss12-12-2-1s-E1. b) Zoom of the thin section shown in a. c) SEM images of the corresponding ROIs. d) Median grain-size variability according to the ROIs. Red horizontal bars in c) represent varve boundaries made without SEM images. Black rectangles at the left of SEM-images in c represent clay caps. e) Thin section SS12-12-2-1s D2 covering ~1600 CE – 1608 CE at 58.2 cm–62.5 cm composite depth. Three thick successive layers are observed. Red squares represent the two SEM images. f) and g) show a SEM-image of a clear clay cap (f) and a successive layer (g). (For interpretation of the references to colour in this figure legend, the reader is referred to the Web version of this article.)

deposited during winter, when lakes are typically covered by at least 2 m of ice. Consequently, these layers are considered as making part of one single varve year. Hence, the backscatter electron (BSE) images give a more detailed view of sedimentation processes in the lake and thus help to delineate varves more precisely. These features were observed in intervals at 25.6–26.6 cm, 51.9–52.3 cm, 73.6–75.2 cm, 251.3–251.9 cm and 253.1–255.8 cm of the composite depth. These intervals are illustrated in Fig. S2.

Intervals where successive, thick graded layers (>10 mm) occur have more variable varve counts. These facies are characterized by coarser grain-size at their base and an upward fining sequence. It can be difficult to clearly identify whether these layers are the top of a turbidite sequence, a winter clay cap from a thick varve, or a sub-annual layer formed from a heavy summer rain event. As pointed out by Zolitschka et al. (2015), these features, which are related to a change in sedimentation rate, are hard to distinguish because they may be the result of several different hydrological events within the same season (e.g. rainfall, snowmelt, mass movement events). As an example, Fig. 3e shows a thin section highlighting three successive thicker layers (>1 cm). As shown in the BSE SEM images (Fig. 3g), there is a decrease in grain-size variation toward the top of the layer while the layer above it contains coarser material. Based only on the digital image of the thin section, these can be interpreted as being individual annual layers, which is most likely the case for the upper SEM image (Fig. 3f). However, in the case of the lower SEM image (Fig. 3g) there is no obvious presence of a clay cap, and indeed this is more likely to be a successive layer event from the same year (Fig. 3g). Such successive layers occur only six times in the whole varved record (at 58.2 cm–63.8 cm, 105.8–107.7 cm, 107–108 cm, 110.3–112.2 cm, 129.2–131.7 cm, and 269–272.3 cm of the composite depth; see Fig. S3). Overall, the laminated sediments are unambiguous and well defined in the upper 4.9 m.

3.2. Composite sequence of the SSL varve record

The composite sequence is based on 100 thin sections extracted from nine overlapping core sections to obtain the most reliable continuous record (Fig. S1). One count was performed using thin-sections scans/photographs only, and three counts were made using SEM images. A total of 2900 varve years were identified (Figs. 4–6) in which 37 stratigraphical markers (beds thicker than

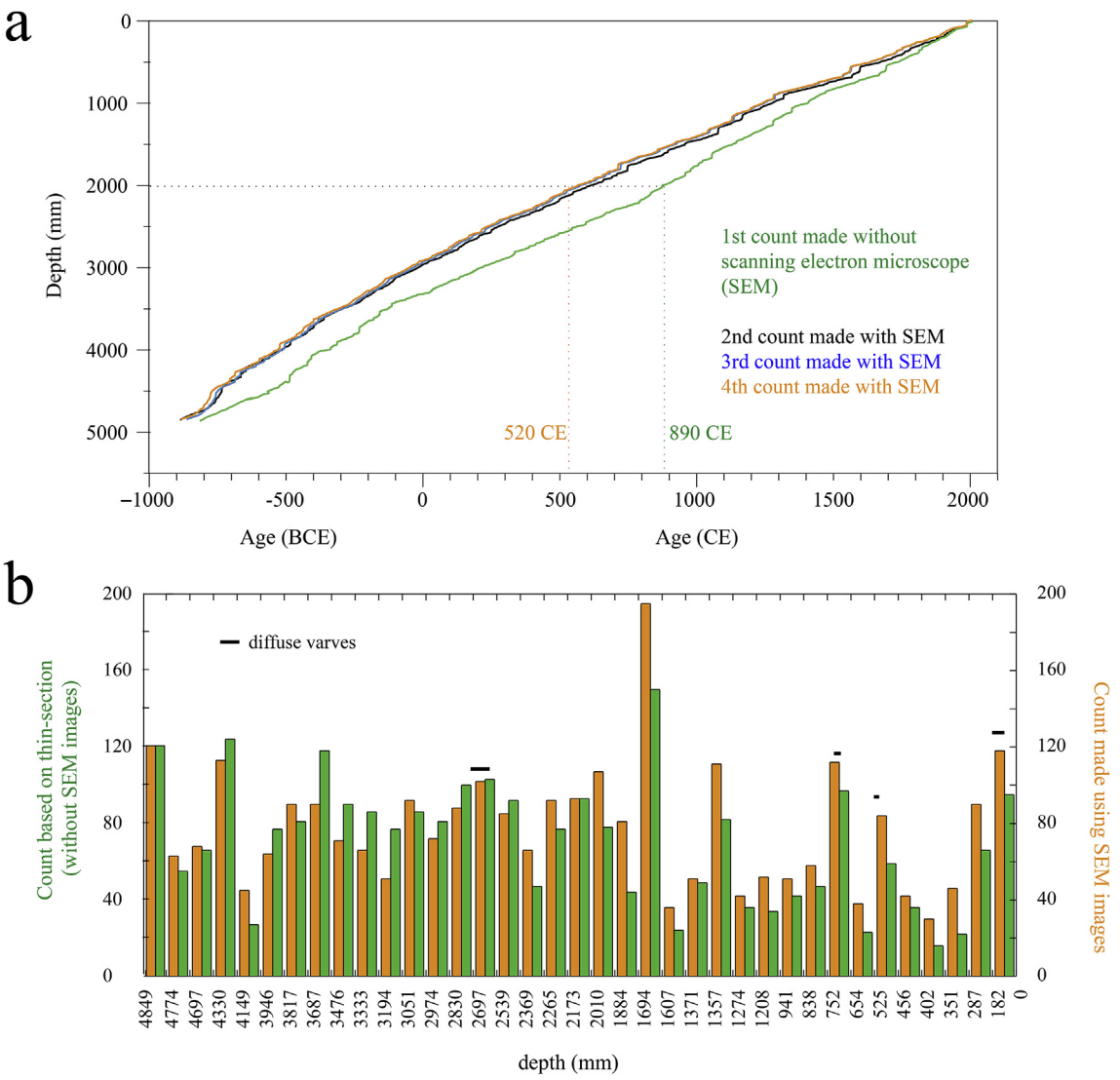

Fig. 4. a) Four different varve counts: 1st made without the use of scanning electron microscope (SEM) images (green); 2nd to 4th are counts made using SEM images. b) Differences in varve counts between the 4th count made with SEM (orange) and the count made without SEM (green) versus depth. Black horizontal rectangles identify diffuse varves seen in the varve chronology. (For interpretation of the references to colour in this figure legend, the reader is referred to the Web version of this article.)

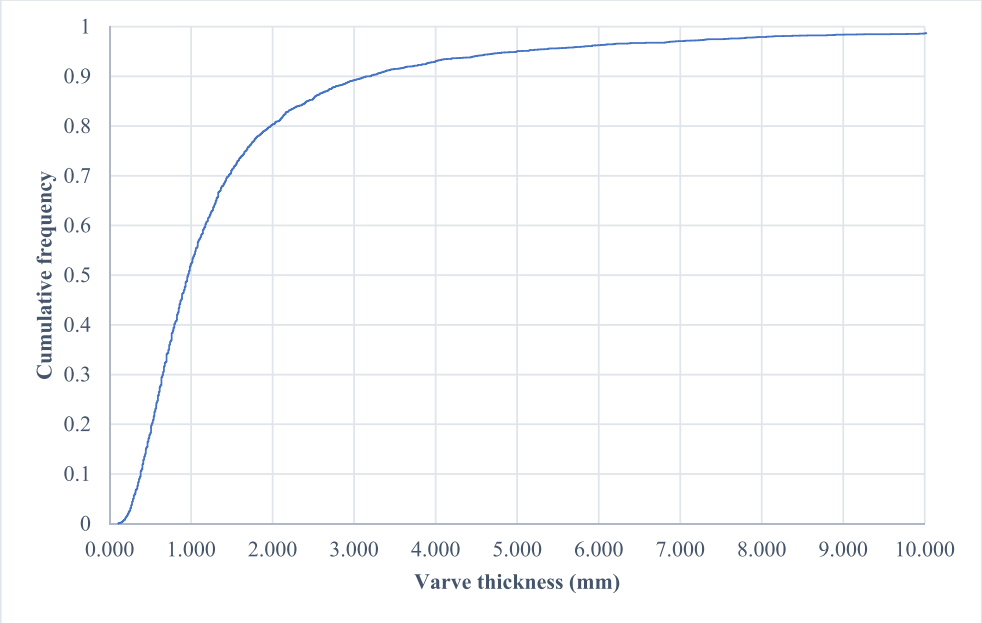

Fig. 5. Cumulative frequency of the varve thickness series. Note that half of the varve thicknesses are less than 1 mm.

0.8 cm) were used to compare varve counts between these layers (Fig. 4b). The three counts made using SEM images yield similar results with an overall difference of only 36 varves between the counts, or an estimated error of 1.2%, indicating that the varves can be delineated quite accurately (Fig. 6). Some discrepancies occur in those rare sections of the varve record that show a more diffuse pattern and when successive layers occur (e.g. Fig. 3). When comparing the varve counts based on optical images of thin sections (using a transparency flatbed scanner at 2400 dpi resolution), to one made using SEM images, the latter resulted in more varves being counted (Fig. 4). While the average varve thickness is 1.67 mm (Table S1), the median varve thicknesses is 0.96 mm (Table S2, Fig. 5), meaning that half of the varves are <1 mm in thickness, which are very challenging to delineate without high-resolution SEM imagery. Cumulative frequency of the varve thicknesses distribution indicates that 90% of the varves are <3 mm thick (Fig. 5). When the density flow deposits (turbidites and debris flow) are excluded from this analysis, the average varve thickness of this time series becomes 1.28 mm, but the median value does not change significantly (0.93 mm).

3.3. Independent chronological control

3.3.1. Radiometric dating

For the upper 18.25 cm, the varve count compares well with the ^{210}Pb CRS chronology over the past 120 years (Fig. 6b). Furthermore, the ^{137}Cs peak in 1963 matches the varve counts when they are shifted by 9 years, which is in agreement with Francus et al. (2002) who concluded that 9 years were eroded by a large basin-wide turbidite dated to 1990. This means that 21 varves were deposited between 1990 and May of 2012 when the cores were collected, providing additional evidence that this record is annually laminated.

3.3.2. Optically stimulated luminescence (OSL) dating

OSL dating of quartz grains for four samples from the cores further constrain the varve chronology (Table 1). The grains that yielded the OSL age of 7630 ± 595 BP (5620 BCE) were sampled beneath the laminated section and above high-energy layers (core SS12-12-2-3P) that are likely related to pulses of a melting glacier, in what appears to be a transitional period between the retreat of glacier in the watershed and the subsequent inception of the lake (Fig. 6d – black rectangle). This age (~5620 ± 595 BCE) is considered to be reliable since the region is believed to have been fully deglaciated around ~5800 BCE (England, 1983). Moreover, it has low overdispersion (22%) and this age remained unchanged at one sigma error with the addition of aliquots, and has a unimodal population of equivalent dose. Thus, the age ~5620 ± 595 BCE can be viewed as secure. The OSL age centered at 2720 (710 BCE), located close to onset of lacustrine infill, agrees at one sigma error with the varve chronology (674 BCE ± 28) (Fig. 6a and 6d – green rectangle). Two other OSL ages centered at 1260 and 960 year (750 CE and 1050 CE) have the highest overdispersion and are likely less reliable. This could be due to problems specific to the dating of young sediments. Because younger sediments are less unconsolidated and less dewatered, they are characterized by insufficient luminescence sensitivity to allow measurements at very low doses (~tens of mGy) which results in a low signal to noise ratio and imprecise doses. Hence, the age of such sediments are often underestimated (Madsen and Murray, 2009). This might be the case here as the estimated OSL dates are too young compared to our varve chronology (368 CE ± 26 and 509 BCE ± 28). Therefore, the two upper OSL dates have been disregarded. Overall, OSL dating provided only chronological control for the basal core sample into the underlying glacial-fluvial deposit but yielded overestimates in the overlying sediments.

3.3.3. Paleomagnetic variations

Variations of the inclination recorded in the South Sawtooth Lake sediments reveal similar patterns when compared to Lower Murray Lake (Fig. 7, r = 0.45) located 320 km northeast of SSL (LML: Fig. 1a). Intervals where the records are different correspond to thicker than normal layers (normal being <3 mm which represents 90% of the varve thicknesses) in the SSL record. Two examples of density flow deposits dated to ~690 CE and ~750 BCE are shown in Fig. 7. In these sedimentary facies, fine to medium sand is found at

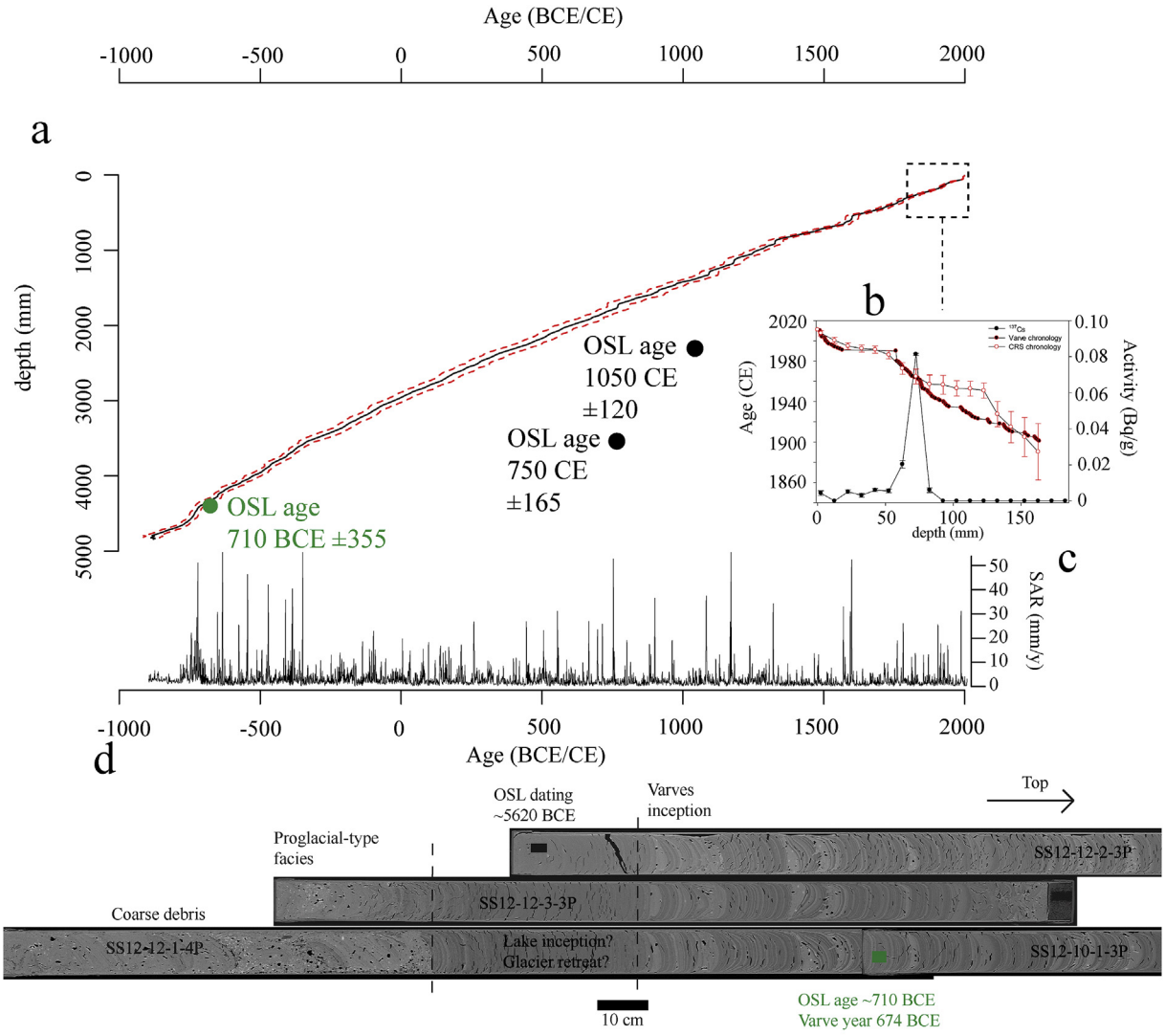

Fig. 6. a) Age model based on the three counts using SEM images. The red lines delimit the one standard deviation and the black line is the count average. Overall sedimentation rate is 1.67 mm a^{-1}. b) ^{137}Cs activity, ^{210}Pb dating and varve count against depth. c) Sediment accumulation rates (mm a^{-1}) based on the mean age-depth shown in a). d) Ct-Scan of sediment cores SS12-12-2-3P, SS12-12-3-3P, SS12-10-1-3P and SS12-12-1-4P with the location of 2 samples extracted for OSL dating (black and green rectangles). (For interpretation of the references to colour in this figure legend, the reader is referred to the Web version of this article.)

184.7 and 472.3 cm composite depth, which explains the sharp decrease in inclination values, as reported by St-Onge et al. (2004) and Valet et al. (2017). When all of the 38 density flow layers are removed from the analysis, the correlation coefficient slightly increases (R = 0.48 without density flows).

3.3.4. Discussion about the varve chronology

Radiometric dating (^{210}Pb) shows excellent agreement with the varve chronology for the past ~120 years. For longer time scales, as radiocarbon dating is often not reliable in this type of Arctic environment (Abbott and Stafford, 1996), we looked for alternative dating methods. Amongst them, samples were extracted for tephrochronology to target the 1362 CE Icelandic volcanic event. Unfortunately, this attempt was not successful. First, SSL is far from any volcanic source (>2500 km), unlike the western American coast, where abundant cryptotephras have been found because of the proximity of volcanic sources (e.g. Deschamps et al., 2018). Second, SSL sediments are 99% clastic which makes the extraction of tephra challenging. So far, no lacustrine varve records in the Eastern Canadian Arctic Archipelago have been validated using tephrochronology to identify a known volcanic event in the Eastern Canadian Arctic Archipelago. The generally strong co-variability between the SSL paleomagnetic record and the one from LML (Cook et al., 2009) supports the SSL varve age model. Indeed, the chronology of LML, through its paleomagnetic variations, was also confirmed by a well-dated marine sediment archive from Disraeli Fjord, Ellesmere Island (Antoniades et al., 2011). The age of ~710 BCE obtained from OSL dating is similar to the paleomagnetic variations of both SSL and LML providing further support for the chronology in the latter part of our record.

3.4. Sediment facies properties

3.4.1. μ-XRF and physical composition of varves

Correlation matrix of the elemental composition and the Houndsfield units (HU) is shown in Fig. 8 and Table S4. The inc/coh is defined by the Compton (incoherent) and Rayleigh (coherent) scattering ratio. Negative correlation between inc/coh and HU indicates that inc/coh can be used as a density proxy (r = −0.58), as was found by Guyard et al. (2007) and Fortin et al. (2013). Sr and Rb

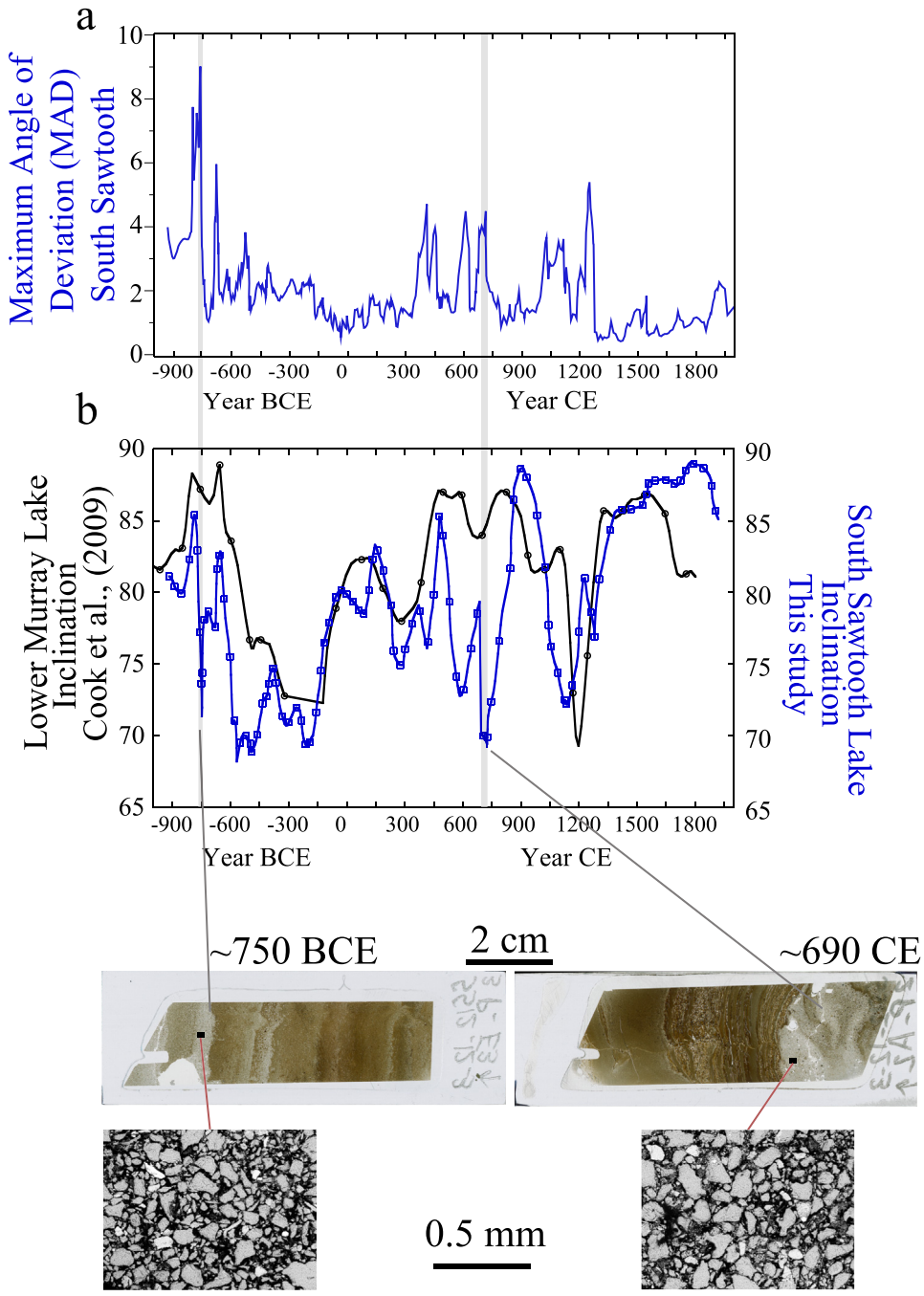

Fig. 7. Comparison of South Sawtooth and Lower Murray Lakes paleomagnetic inclination records. Below: two thin sections (left: SS12-12-3-3P-E3 and right: SS12-12-3-2P-A2) showing thick layers with bright coarse sediments (highlighted by two gray bars). South Sawtooth Lake inclination data are filtered by a 10-point centered moving average to compare to the lower resolution at Lower Murray Lake. Note that the paleomagnetic data of SSL are plotted here against this new chronology, while the Lower Murray Lake data are plotted according to its original chronology (Cook et al., 2009).

are strongly correlated to each other (Fig. 8 and Table S4, r = 0.84). Sr and Zr are also well correlated (r = 0.61) and K is rather poorly correlated to most of the other elements, except for Rb (r = 0.40). As for Fe and Mn, which are often used as a paleo-redox proxy, it can be observed that Fe is highly dependant on detrital input since it is correlated to Ti, while Mn is correlated to inc/coh (and HU).

A similar co-variability is observed between inc/coh, HU, Zr, Ti, Si and Ca, as shown in Fig. 9. However, Zr increases sharply at the base of high-energy events as observed in the various darker layers (Fig. 9a and b). This pattern is similar to other studies which show that Zr is enriched in coarser grain deposits as Zr is associated with heavy and hard minerals (Scheffler et al., 2006). This is further confirmed by the backscatter SEM images showing Zr enriched in coarse silt to very fine sand layers according to the classification of Folk and Ward (1957) (Fig. 9c). The main lithology found where the main inflow is located consists of sandstones interstratified with siltstones, and shales with minor amounts of coal. Thus, quartz are a major component of the sediment at Sawtooth Lake. This can be

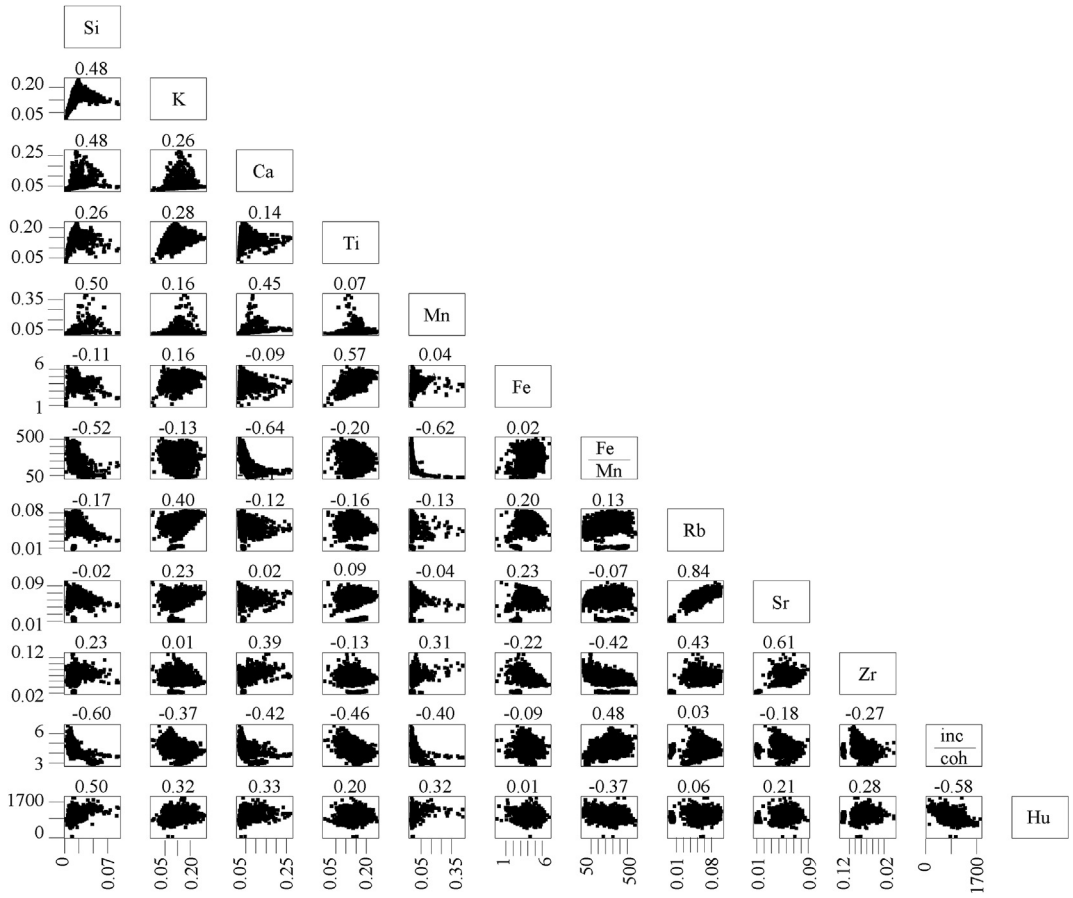

Fig. 8. A) Scatter plots of the elements at South Sawtooth Lake with CT-Scan Houndsfield Units. All resampled data points represent a value integrated over 2 mm (2605 data points per dataset).

observed by the strong co-variability of Si and Zr at the base of many coarse layers (Fig. 9). Ti is also known to be linked with clastic input, mainly found in fine to medium silty layers, as has been reported in many sites (Balascio and Bradley, 2012; Cuven et al., 2010; Kylander et al., 2011; McWethy et al., 2010). Both Ti and Zr relate to beds with grain-sizes coarser than average, but in graded beds such as turbidites. Ti has lower concentrations at the base of turbidites, but increases sharply in thicker layers as the grain-size becomes finer, just when Zr starts to decrease upward (Fig. 9). Particle size distribution reveals that Ti is enriched in the medium silt layers (Fig. 9c). In general, inc/coh, Ti and HU display similar trends and are at higher concentration in high-energy events layer (turbidites), which is also the case for Si and Ca. These results are consistent with a previous study on a long sediment sequence from Patagonia showing that CT-Scan (HU) and inc/coh provide high-resolution and reliable measurements of sediment density variability (Fortin et al., 2013).

3.4.2. Stratigraphic trends of sediment properties

A general feature in the evolution of the grain-size indices is the overall declining trend in values from 900 BCE until the beginning of the 20th century, when most values increased with the exception of varve thickness (Fig. 10 and S5, Table S5). This is especially evident in the 50th percentile of grain-size showing high values during the 20th century and the coarsest grain-size in 1990 relative to the past 2900 years (Fig. 10a). This general decreasing trend in grain-size is most visible when a 11 year-running mean is applied to the series (Fig. 10b). These physical parameters exhibit many common features as shown in the correlation matrices (Table S3). Some of them show similar characteristics found in a varve record from Cape Bounty, at East Lake (CBEL) (Lapointe et al., 2012). For example, the median (D50) is the grain-size index that exhibits the best correlation with varve thickness ($r = 0.42$). Similarly, the 99th percentile (D99) is strongly correlated with the standard deviation sD_0 ($r = 0.92$) as was observed at Cape Bounty East Lake (Lapointe et al., 2012).

The general trend of the annual μ-XRF variations reveals in general a decrease in values from 900 BCE to present (Fig. 10a). This is consistent with the particle size data (Fig. 10a, S5). For example, Ti and Zr values show a decreasing trend through time, which is also reflected in inc/coh (inverted values) and relative density data from the Ct-Scan. We also note that the recent (~1850 CE) increase in Zr is not as noticeable as that of the coarse grain-size data. While a substantial decreasing trend of Zr around 1500s-present is observed, Ca variability shows an increase trend during that time (Fig. 10a). The overall correlation between Ca and Zr is significant ($r = 0.39$, $p < 0.0001$). However, when taking into account only the past 500 years, a negative correlation is found ($r = -0.32$, $p < 0.0001$).

3.4.3. Discussion about the stratigraphic trends

The increase in Ca profile on the top of the record appears to point to a different source of sediment provenance to the lake over the past ~500 years. The lithology in direct contact with the lake located in the col within the Sawtooth Range consists of sandstones and calcareous siltstones, with limestones and shales (Geological

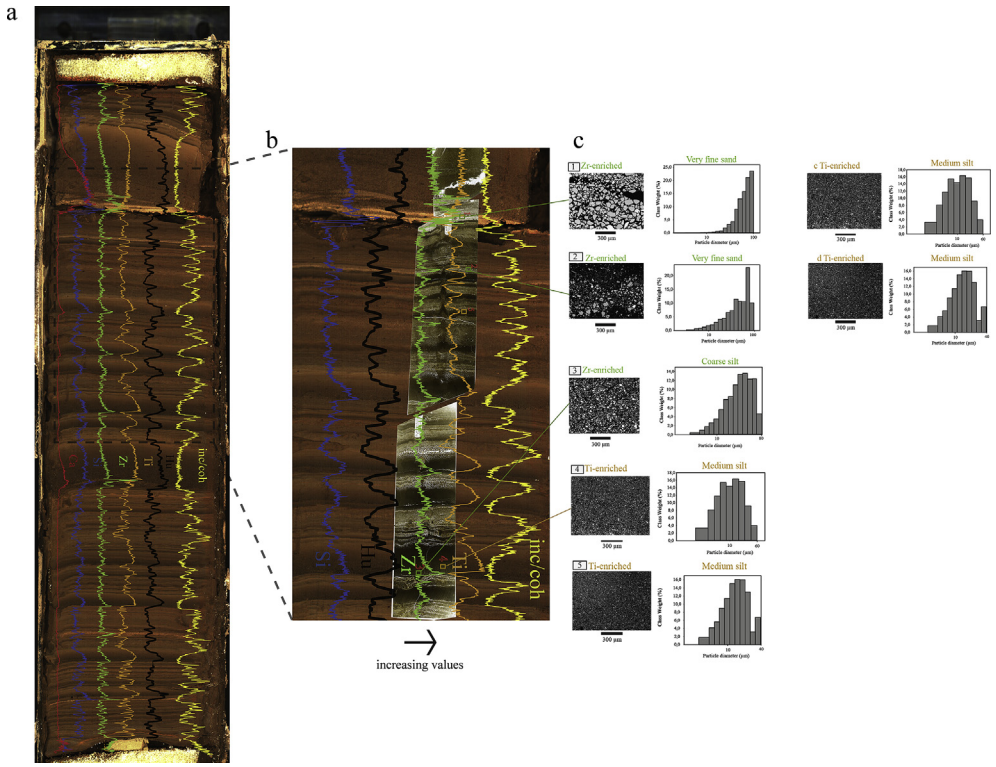

Fig. 9. a) Gravity core SS12-1-1s from SSL showing μ-XRF variations of inc/coh (yellow), Houndsfield Unit (HU; black), Titianium (orange), Zirconium (green), Silicium (blue) and Calcium (red). b) Blow-up (gray dashed line of a) showing inc/coh, Titianium, Zirconium, HU and Silicium. The arrow indicates increased values of the parameters shown. Squares labeled from 1 to 5 are regions of interest photographed at the Scanning Electron Microscope in backscatter mode (c). c) Backscatter scanning electron microscope images of the 5 rectangles shown in b with their grain-size distribution. Scanning electron microscope images highlighting coarse silt and fine sand enriched with Zr and medium silt sediment enriched in Ti. (For interpretation of the references to colour in this figure legend, the reader is referred to the Web version of this article.)

Survey of Canada, 1972). It is thus possible that the increase in Ca over the past 500 years is linked with more sediment deposition from this col area where steep slopes and gullies are present (Fig. 1c). Francus et al. (2008) hypothesized that sedimentation from that source was expressed as debris flows triggered by summer rain events. These events produce thin yet coarsed grained layers. Hence, coarse grain-size and Ca increase during the course of the last 100 years would mean that summer rain events became more frequent, an interpretation consistent with a warming climate. The upward decline of the Zr profile suggests that the relative importance and frequency of snow-melt induced turbidites originating from the main river watershed that is mainly composed of sandstones and siltstone have declined over the past 100 years. Overall, the results reveal that μ-xrf and particle size measurements contain different information that can inform the interpretation of paleoenvironmental conditions.

Changes in grain-size mainly reflect changes in snow melt intensity (Francus et al., 2002) that are influenced by the length of the ice-free season, and therefore summer temperature. This general decreasing trend in grain-size might thus be attributed to the decrease of northern hemisphere insolation during the past ~6ka which led to lower hydrological energy-events available to move sediment in the SSL main river, resulting from lower snow melt intensity due to decreased temperature (Francus et al., 2002; Kaufman et al., 2004). The finer fraction (<16 μm) increased from ~1200 CE until 1850 CE (Fig. S5), a period that corresponds broadly to the Little Ice Age (LIA). The increase in coarse grain-size in the 20th century occurs during a similar time interval to the period of pronounced warming shown in reconstructed Arctic temperature (Kaufman et al., 2009). Indeed, the long-term declining trend in coarse grain-size has been recently sharply reversed (Fig. 10b). Another varved sediment record in the Western Canadian Arctic, from Cape Bounty East Lake (CBEL) also recorded coarse grain-size values during the 20th century that reached unprecedented levels (Lapointe et al., 2012). These changes clearly show that these records are sensitive indicators of temperature fluctuations. Other periods such as ~800 BCE and ~650-700 CE in the SSL record also depict strong coarse grain-size anomalies that are higher than today.

Another interesting trend is that varve thickness in the recent part of the record did not increase at the same pace as the coarse grain-size fraction, another result that is also seen in the varved record from the western Canadian Arctic (CBEL). Indeed, correlation between most of the grain-size data and varve thickness is statistically significant but the strength of the correlation is nevertheless rather weak (Table S3). The reasons that explain these incompatibilities between the coarse grain-size and varve thickness are not fully understood. Clearly, thicker varves do not always reflect greater grain-size (Lapointe et al., 2012, Fig. S6). This might be related to the fact that a varve year can result from multiple successive snowmelt events with low energy that prevent the transport and deposition of coarser material (Fig. S6). Conversely, the increase in coarse grain-size and Ca in the past ~100 years may be linked to more frequent debris flow triggered by summer rainfall that are not necessarily characterized by thick layers as mentioned above.

3.5. Comparison of Sawtooth record to meteorological and paleoclimate data

PCA analysis indicates that annual sediment elemental variations are different than grain-size measurements (Fig. 11). The first

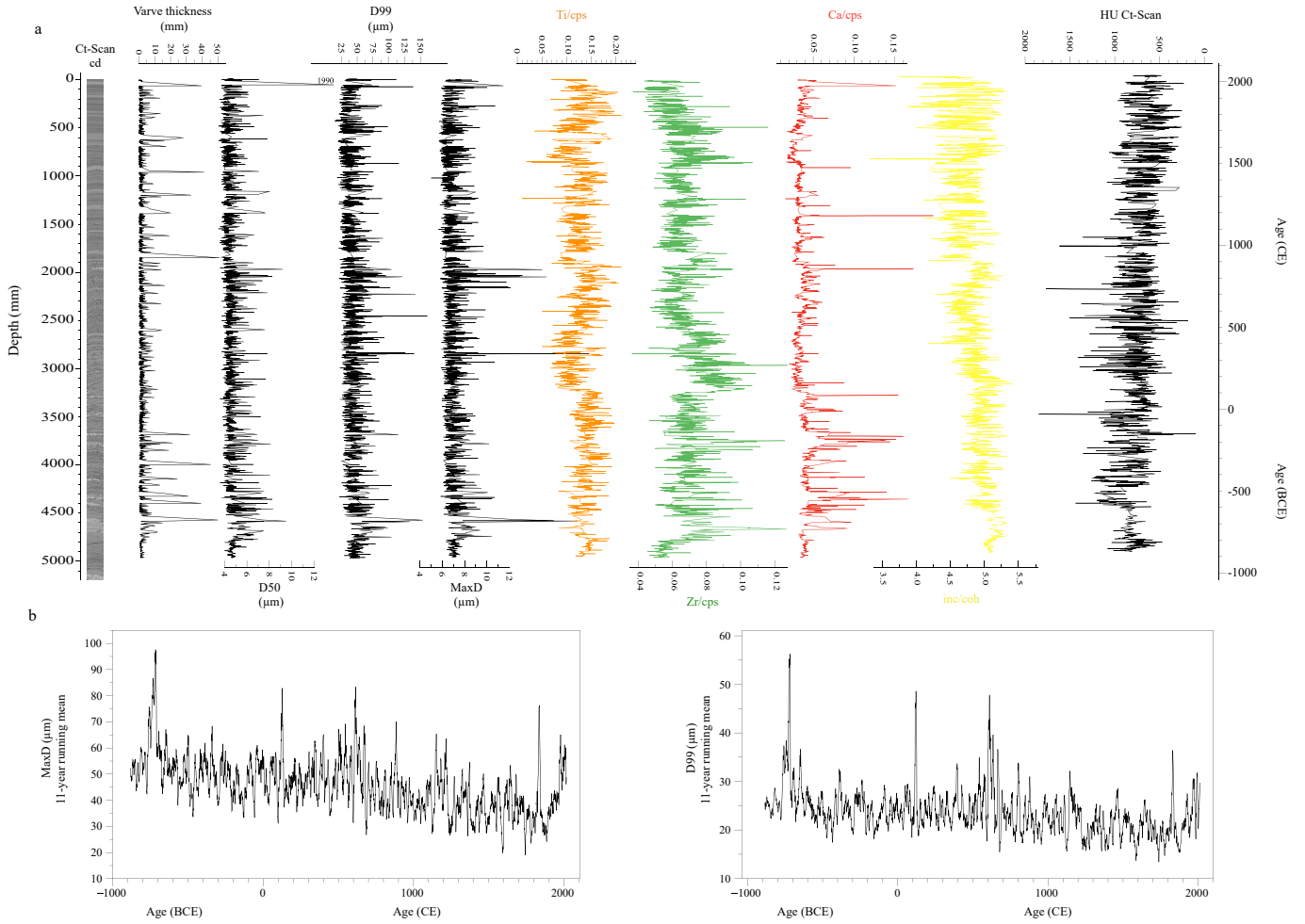

Fig. 10. a) Composite Ct-Scan image of the first ~5 m with grain-size parameters, varve thickness, grain-size data (50th percentile, 99th percentile and the Maximum diameter), μ-XRF data and Ct-Scan from South Sawtooth Lake over the past 2900 years. b) $MaxD_0$ and D99 over the past 2900 years filtered by an 11-year centered running mean.

principal component (related to coarse grain-size) explains 26% of the variability whereas the second component (μ-XRF) accounts for 16% of the variability. However, some modest but significant correlations between grain-size, XRF, and Ct-Scan density suggest a common sources of variability among the proxies (Table 2).

Ti and finer particle size (% < 20 μm) are significantly correlated to PC2 ($r = 0.87$, $p < 0.0001$, $r = 0.39$, $p < 0.01$), but moderately anti-correlated to PC1 ($r = -0.33$, $p = 0.007$, $r = -0.79$, $p < 0.001$) over the period of instrumental data (Table S5) (Ti vs PC2 over the past 2900 years: $r = 0.68$, $p < 0.0001$). The strongest correlation for the PC1 is obtained with D99 ($r = 0.96$, $p < 0.0001$) (D99 vs PC1 over the past 2900 years: $r = 0.90$, $p < 0.0001$). These results indicate that PC1 reflects coarser grain-size while PC2 is more related to finer particle size as shown by the significant positive correlation with the fraction <20 μm, and <30 μm (Table 3).

These data were then compared to the Eureka weather station located at 84 km north-west of SSL (Fig. 1a). D99 and PC1 (coarse grain-size) are significantly and positively correlated with May to August temperature from 2011 to 1948 AD (Table 3). An opposite pattern is observed with PC2 (and Ti) which shows a strong negative link to temperature ($r = -0.49$, $p < 0.001$). The variable *snow after 1st of June* (SAJ) is defined as the number of days with snow on the ground following 1st of June. It shows a strong negative correlation with temperature ($r = -0.60$, $p < 0.0001$), indicating that colder conditions preserve the snow in the area. The snow melt intensity (SMI) is defined as the maximum snow depth decrease for a period of 10 days. As shown in Francus et al. (2002), SMI is more an expression of the rate of change from cold to warm days, and tends to be correlated to the subsequent duration of summer snow cover (correlation between SMI and SAJ: $r = 0.33$, $p < 0.001$). Thus PC2 is linked to increased SMI characterized by fine to medium silt deposition in the lake, and thus a proxy for nival melt (Francus et al., 2002), whereas PC1, characterized by coarser grain-size and debris flow, appears more related to increasing temperature (Figs. 10, 12).

PC1 of the multi-proxies at SSL was compared to the average Agassiz $\delta^{18}O$ (Fig. 12b). The $\delta^{18}O$ from ice cores is linked to temperature (Jouzel et al., 1997), but also influenced by changes in moisture source, moisture transport pathways, and precipitation seasonality (Jouzel et al., 1997, Masson-Delmotte et al., 2005, Vinther et al., 2008). A significant correlation is observed during the last 2900 years between PC1 at SSL and $\delta^{18}O$ Agassiz record ($r = 0.65$, $p < 0.001$). Thus, although PC1 and coarse grain-size are moderately correlated to temperature during the instrumental record (Table 3), their long-term variability is similar to the temperature record from Agassiz demonstrating a relatively good proxy for temperature change on Ellesmere Island.

Maximum grain-size diameter ($maxD_0$) and the 99th percentile also show strong co-variability to the Agassiz $\delta^{18}O$ (Figs. 12, S7). The long-term decline of both records is consistent with the progressive

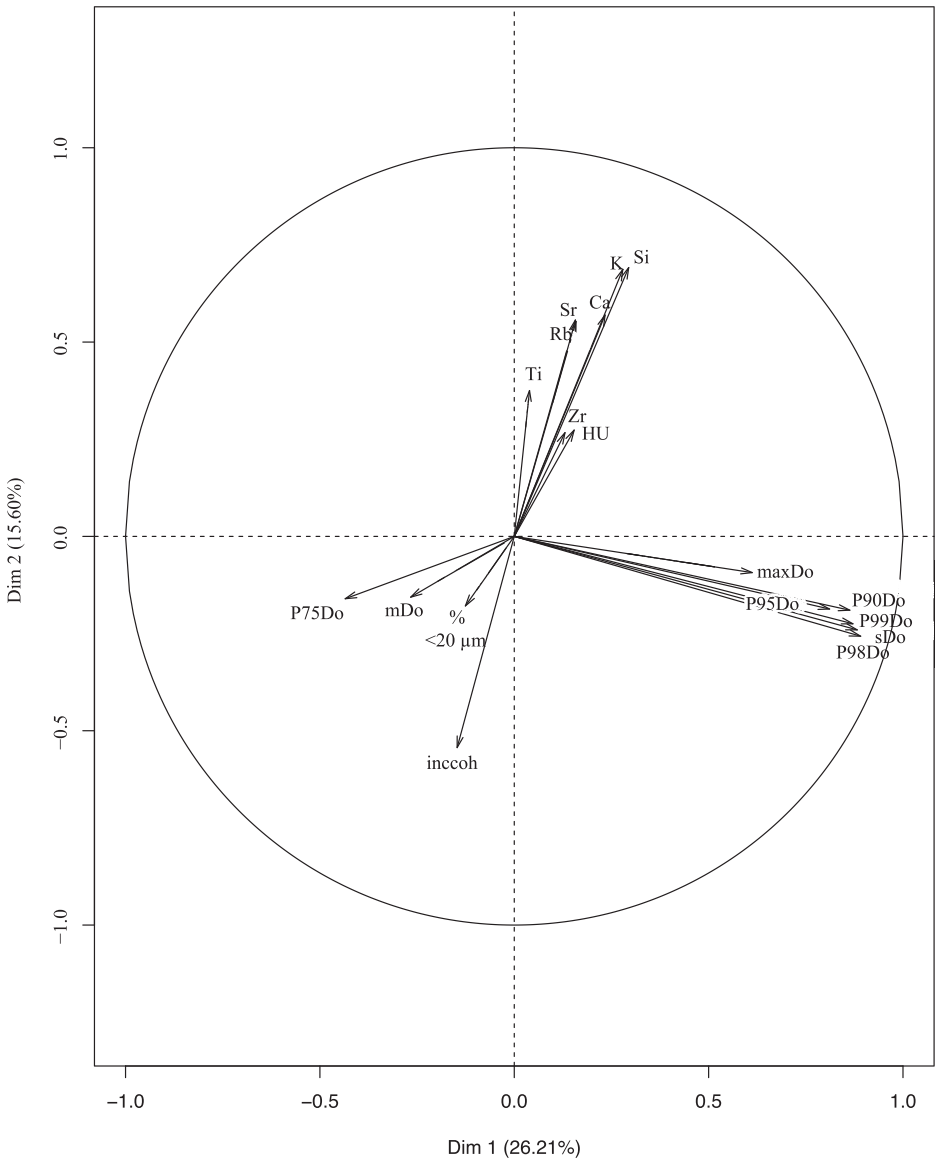

Fig. 11. Principal components analysis (PCA) of density measurements (inc/coh, HU) and other physical parameters shown in this study. Annual data were normalized relative to the mean and standard deviation.

Table 2
Correlation matrix (Pearson) between annual grain-size, Ct-Scan and XRF data over the past 2900 years (A 5-year running average applied to the series to remove noise). Bold values indicate significance <0.05.

	Ti	Zr	Ca	K	Sr	Rb	Si	Hu	inccoh	D50	maxD	D75	D99	>33 µm
Ti	**1**	**−0.34**	**0.39**	**0.49**	0.02	**−0.13**	**0.64**	**0.09**	**−0 52**	**0.07**	0.02	0.04	−0.04	−0.03
Zr	**−0.34**	**1**	**0.09**	**−0.25**	**0.57**	**0.41**	**−0.16**	**0.08**	**−0.30**	**0.20**	**0.21**	**0.17**	**0.20**	**0.12**
Ca	**0.39**	**0.09**	**1**	**0.51**	0.06	**0.08**	**0.64**	**0.18**	**−0.43**	**0.32**	**0.26**	**0.28**	**0.23**	**0.12**
K	**0.49**	**−0.25**	**0.51**	**1**	**0.20**	**0.49**	**0.85**	**0.34**	**−0.48**	**0.29**	**0.42**	**0.28**	**0.32**	**0.42**
Sr	0.02	**0.57**	0.06	**0.20**	**1**	**0.81**	**0.09**	**0.22**	**−0.55**	**0.16**	**0.17**	**0.12**	**0.07**	0.05
Rb	**−0.13**	**0.41**	**0.08**	**0.49**	**0.81**	**1**	**0.21**	**0.32**	**−0.43**	**0.20**	**0.28**	**0.17**	**0.16**	**0.15**
Si	**0.64**	**−0.16**	**0.64**	**0.85**	**0.09**	**0.21**	**1**	**0.25**	**−0.60**	**0.37**	**0.38**	**0.34**	**0.34**	**0.14**
Hu	**0.09**	**0.08**	**0.18**	**0.34**	**0.22**	**0.32**	**0.25**	**1**	**−0.29**	**0.17**	**0.26**	**0.15**	**0.20**	**0.15**
inccoh	**−0.52**	**−0.30**	**−0.43**	**−0.48**	**−0.55**	**−0.43**	**−0.60**	**−0.29**	**1**	**−0.32**	**−0.28**	**−0.29**	**−0.23**	**−0.09**
D50	**0.07**	**0.20**	**0.32**	**0.29**	**0.16**	**0.20**	**0.37**	**0.17**	**−0.32**	**1**	**0.55**	**0.95**	**0.66**	**0.16**
maxD	0.02	**0.21**	**0.26**	**0.42**	**0.17**	**0.28**	**0.38**	**0.26**	**−0.28**	**0.55**	**1**	**0.55**	**0.82**	**0.29**
D75	0.04	**0.17**	**0.28**	**0.31**	**0.12**	**0.17**	**0.34**	**0.15**	**−0.29**	**0.95**	**0.55**	**1**	**0.68**	**0.17**
D99	−0.04	**0.20**	**0.23**	**0.32**	**0.07**	**0.16**	**0.34**	**0.20**	**−0.23**	**0.66**	**0.82**	**0.68**	**1**	**0.29**
>33 µm	−0.03	**0.12**	**0.12**	**0.22**	**0.05**	**0.15**	**0.14**	**0.15**	**−0.09**	**0.16**	**0.29**	**0.17**	**0.29**	**1**

Table 3
Correlation matrix of selected proxies at SSL including PC1 and PC2 compared to meteorological data from Eureka weather station 1948–2011 (Bold values are significant at p = 0.05).

	PC1	PC2	Ti	D99	<20 μm	<30 μm	>30 μm	>60 μm	May–Aug Temp	SMI
PC1	**1**	**−0.33**	−0.16	**0.96**	**−0.81**	**−0.79**	**0.79**	**0.65**	**0.36**	**−0.30**
PC2	−0.33	1	**0.87**	−027	**0.40**	**0.39**	**−0.31**	−0.19	**−0.49**	**0.31**
Ti	−0.15	**0.87**	**1**	−0.15	0.19	0.20	−0.12	−0.23	**−0.48**	**0.32**
D99	**0.96**	−0.08	−0.15	1	−0.81	−0.79	0.76	0.55	**0.38**	**−0.33**
SMI	**−0.30**	**0.31**	**0.32**	**−0.33**	**0.35**	**0.34**	**−0.32**	**−0.36**	−0.21	**1**
Snow depth	0.09	0.10	−0.01	−0.06	0.16	0.06	−0.07	−0.11	023	0.20
Rain	−0.19	0.01	−0.05	−020	0.18	0.18	−0.18	−0.21	−0.05	0.19
May–Aug Temp	**0.36**	**−0.49**	**−0.48**	**0.38**	**−0.30**	**−0.52**	**0.25**	0.19	1	−0.21
Snow after 1st June	−0.18	**0.39**	**0.42**	−0.17	0.29	**0.30**	−0.20	**−0.33**	**−0.60**	**0.33**

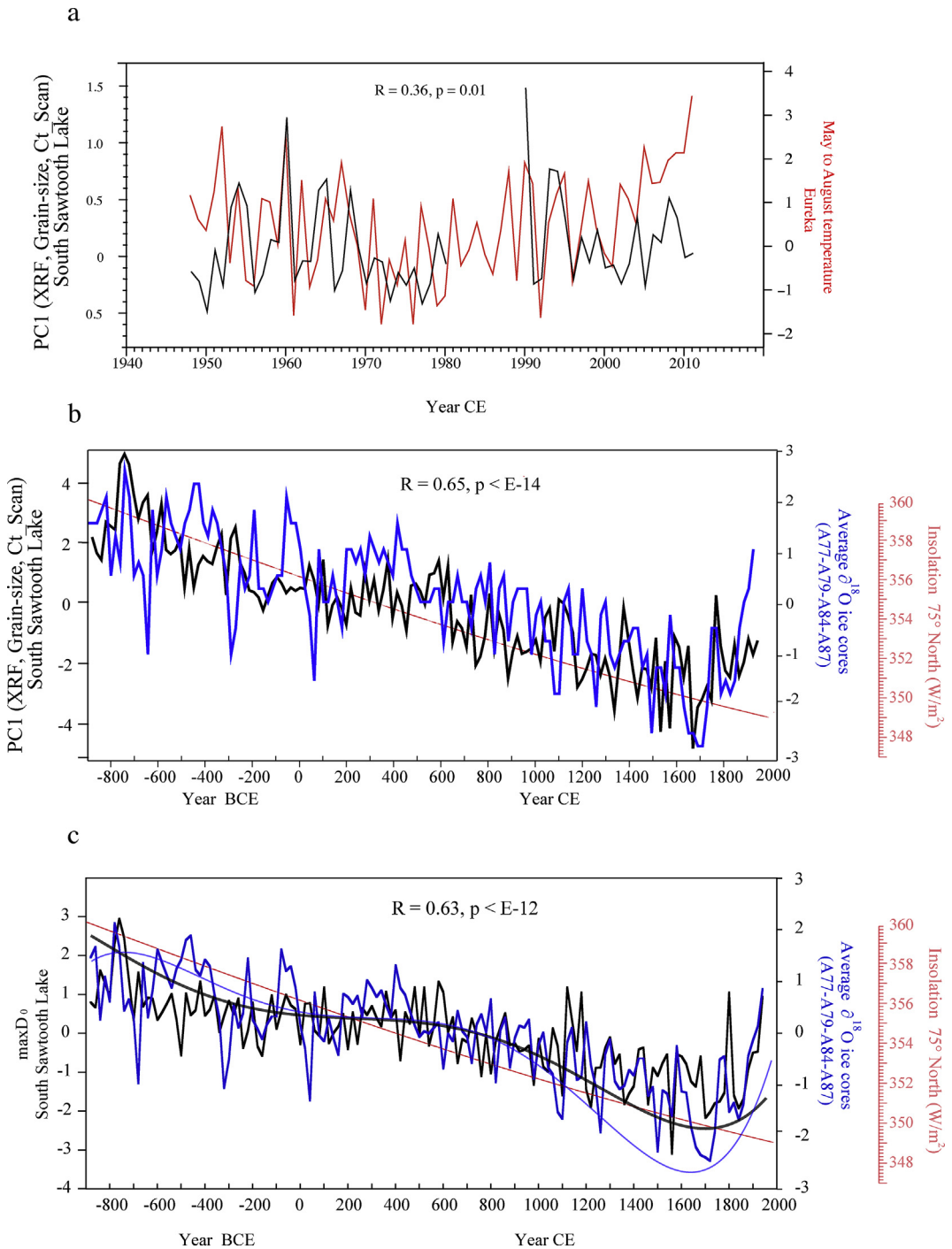

Fig. 12. a) Comparison between South Sawtooth Lake PC1 (μ-XRF data, HU, maxDo, D50 and D99) and May to August temperature data from Mould Bay weather station. b) Same as a) but comparing PC1 with Agassiz ∂^{18}O (mean of A77-A79-A84-A89 ice cores; Fisher et al., 1995). c) same as b) but using the maxD_0 grain-size at South Sawtooth Lake. Black and blue curves in c are the 5th polynomial degree fit at SSL and Agassiz, respectively. (For interpretation of the references to colour in this figure legend, the reader is referred to the Web version of this article.)

decrease in northern hemisphere summer insolation at 80°N due to orbital changes (Fig. 12). However, this declining trend increased after ~700 CE and reached minimum values during the LIA, whereas the older part of the record shows no such trend (Figs. 12, S7a). This pattern is similar to the overall Arctic Holocene temperature variation from the 22 sites located north of 66°N (Briner et al., 2016). Coldest conditions dominated during the LIA and appear to have reached lowest values during the early 18th century (Fig. 12), which is also evident from the finer fraction of grain-size (Fig. S5, % < 16 μm). These lower grain-size values during the LIA likely reflect less transport energy during that cold period. By contrast, the sharp increase of coarse grain-size at the turn of the 20th century is coherent with the reconstructed Arctic temperature showing that recent warming has reversed the long-term cooling trend (Kaufman et al., 2009).

4. Conclusion

This paper presents a new varve chronology from South Sawtooth Lake (SSL), Ellesmere Island, in the Canadian High Arctic, based on high-resolution varve counting. The varve chronology is supported by several independent dating methods, namely the ^{210}Pb and ^{137}Cs profiles, one OSL date, and paleomagnetic comparison with Lower Murray Lake on northern Ellesmere Island (Cook et al., 2009). Furthermore, correlations between the SSL record and the nearby Agassiz Ice Cap δ^{18}O record provides further support that this chronology is robust and that it can serve as a reference for other archives in the Canadian High Arctic (for both marine and lake sediments) given its high sedimentation rate of 1.67 mm a^{-1}. Compared to the other varved records located in the Canadian High Arctic, sedimentation rates at SSL are the highest reported in this wide region. Although many paleoclimate reconstructions from varved sediments are still based only on varve thickness, the results provided here and in a previous study (Lapointe et al., 2012) demonstrate the value of obtaining annual grain-size data using image analysis. Indeed, the superior contrast that this approach provides clearly helps to detect thin varves and decreases the chances of erroneously counting extra-varves (intra-annual layers) thereby increasing the reliability of varve-based chronologies. Furthermore, obtaining a range of annual grain-size measurements enables more paleoenvironmental information to be extracted from the record. Considering that SEM images were crucial in the delineation of thin varves at SSL to refine the chronology, revisiting other key sites to apply this imaging approach to sedimentary records could increase the value and fidelity of other long-term varve-based proxy climate records. Paleomagnetic fluctuations from this site can also be used as a template for other regional archives where radiocarbon dating has proven to be problematical. This will benefit the community by increasing the temporal reliability of regional climate archives for the past ~3 millennia. Our record also shows strong similarities with the nearby δ^{18}O Agassiz Ice Cap, suggesting that the SSL varved record is sensitive to temperature variability. Finally, this study provides the sedimentological, stratigraphical and chronological basis for future paleoclimatic reconstructions from SSL sediments.

Acknowledgements

We wish to thank the Polar Continental Shelf Program for their field logistic support and NSERC grants to PF and GSO. FL is grateful to grants provided by the W. Garfield Weston Foundation and the Fond Quebecois de la Recherche sur la Nature et les Technologies. We also acknowledge support from NSF grant OPP-1744515 to the University of Massachusetts. Special thanks for Alison MacLeod (University of London) for cryptotephra analysis. FL would also like to thank Alexandre Normandeau for his help with the seismic data. We are thankful for the comments of two anonymous reviewers. Paleo-data used in this study can be found on the NOAA server https://www.ncdc.noaa.gov/data-access/paleoclimatology-data/datasets.

Appendix A. Supplementary data

Supplementary data to this article can be found online at https://doi.org/10.1016/j.quascirev.2019.105875.

References

Abbott, M.B., Stafford, T.W., 1996. Radiocarbon geochemistry of modern and ancient Arctic lake systems, Baffin Island, Canada. Quat. Res. 45 (3), 300–311.
Antoniades, D., Francus, P., Pienitz, R., St-Onge, G., Vincent, W.F., 2011. Holocene dynamics of the Arctic's largest ice shelf. Proc. Natl. Acad. Sci. U.S.A 108 (47), 18899–18904.
Appleby, P., 2002. Chronostratigraphic techniques in recent sediments. In: Tracking Environmental Change Using Lake Sediments. Springer, pp. 171–203.
Balascio, N.L., Bradley, R.S., 2012. Evaluating Holocene climate change in northern Norway using sediment records from two contrasting lake systems. J. Paleolimnol. 48 (1), 259–273.
Bøtter-Jensen, L., Bulur, E., Duller, G., Murray, A., 2000. Advances in luminescence instrument systems. Radiat. Meas. 32 (5), 523–528.
Briner, J.P., McKay, N.P., Axford, Y., Bennike, O., Bradley, R.S., de Vernal, A., Fisher, D., Francus, P., Fréchette, B., Gajewski, K., 2016. Holocene climate change in Arctic Canada and Greenland. Quat. Sci. Rev. 147, 340–364.
Cohen, J., Screen, J.A., Furtado, J.C., Barlow, M., Whittleston, D., Coumou, D., Francis, J., Dethloff, K., Entekhabi, D., Overland, J., 2014. Recent Arctic amplification and extreme mid-latitude weather. Nat. Geosci. 7 (9), 627–637.
Cook, T.L., Bradley, R.S., Stoner, J.S., Francus, P., 2009. Five thousand years of sediment transfer in a high arctic watershed recorded in annually laminated sediments from Lower Murray Lake, Ellesmere Island, Nunavut, Canada. J. Paleolimnol. 41 (1), 77–94.
Croudace, I., Rindby, W.,A., Rothwell, R.G., 2006. ITRAX: description and evaluation of a new multi-function X-ray core scanner. Spec. Publ. Geol. Soc. Lond. 267, 51.
Cuven, S., Francus, P., Lamoureux, S.F., 2010. Estimation of grain size variability with micro X-ray fluorescence in laminated lacustrine sediments, Cape Bounty, Canadian High Arctic. J. Paleolimnol. 44 (3), 803–817.
Deschamps, C.-E., St-Onge, G., Montero-Serrano, J.C., Polyak, L., 2018. Chronostratigraphy and spatial distribution of magnetic sediments in the Chukchi and Beaufort seas since the last deglaciation. Boreas 47 (2), 544–564.
Duchesne, M.J., Moore, F., Long, B.F., Labrie, J., 2009. A rapid method for converting medical Computed Tomography scanner topogram attenuation scale to Hounsfield Unit scale and to obtain relative density values. Eng. Geol. 103 (3), 100–105.
Duliu, O.G., 1999. Computer axial tomography in geosciences: an overview. Earth Sci. Rev. 48 (4), 265–281.
Duller, G., 2003. Distinguishing quartz and feldspar in single grain luminescence measurements. Radiat. Meas. 37 (2), 161–165.
Edlund, S.A., Alt, B.T., 1989. Regional congruence of vegetation and summer climate patterns in the Queen Elizabeth Islands, northwest Territories, Canada. Arctic 3–23.
Fain, J., Soumana, S., Montret, M., Miallier, D., Pilleyre, T., Sanzelle, S., 1999. Luminescence and ESR dating Beta-dose attenuation for various grain shapes calculated by a Monte-Carlo method. Quat. Sci. Rev. 18 (2), 231–234.
Fisher, D.A., Koerner, R.M., Reeh, N., 1995. Holocene climatic records from Agassiz ice cap, Ellesmere Island, NWT, Canada. Holocene 5 (1), 19.
Folk, R.L., Ward, W.C., 1957. Brazos River bar: a study in the significance of grain size parameters. J. Sediment. Petrol. 27 (1), 3–26.
Fortin, D., Francus, P., Gebhardt, A.C., Hahn, A., Kliem, P., Lisé-Pronovost, A., Roychowdhury, R., Labrie, J., St-Onge, G., Team, T.P.S., 2013. Destructive and non-destructive density determination: method comparison and evaluation from the Laguna Potrok Aike sedimentary record. Quat. Sci. Rev. 71, 147–153.
Francus, P., Asikainen, C., 2001. Sub-sampling unconsolidated sediments: a solution for the preparation of undisturbed thin-sections from clay-rich sediments. J. Paleolimnol. 26, 323–326.
Francus, P., Nobert, P., 2007. An integrated computer system to acquire, process, measure and store images of laminated sediments. In: 4th Internat. Limnogeol. Cong. Barcelona, 11-14th July.
Francus, P., Pirard, E., 2004. Testing for sources of errors in quantitative image analysis. In: Francus, P. (Ed.), Image Analysis, Sediments and Paleoenvironments.
Francus, P., Bradley, R.S., Abbott, M.B., Patridge, W., Keimig, F., 2002. Paleoclimate studies of minerogenic sediments using annually resolved textural parameters. Geophys. Res. Lett. 29 (20), 1998.
Francus, P., Bradley, R.S., Lewis, T., Abbott, M., Retelle, M., Stoner, J., 2008. Limnological and sedimentary processes at Sawtooth Lake, Canadian High Arctic, and their influence on varve formation. J. Paleolimnol. 40 (3), 963–985.
Galbraith, R.F., Roberts, R.G., Laslett, G.M., Yoshida, H., Olley, J.M., 1999. Optical

dating of single and multiple grains of quartz from Jinmium rock shelter, northern Australia: Part I, experimental design and statistical models. Archaeometry 41 (2), 339–364.
Geological Survey of Canada, 1972. Geological map, Canon Fiord, District of Franklin, Map 1308A, scale 1:250,000.
Guyard, H., Chapron, E., St-Onge, G., Anselmetti, F.S., Arnaud, F., Magand, O., Francus, P., Mélières, M.A., 2007. High-altitude varve records of abrupt environmental changes and mining activity over the last 4000 years in the western French Alps (lake Bramant, Grandes Rousses Massif). Quatern. Sci. Rev. 26 (19), 2644–2660.
Husson, F., Josse, J. S. Le, Mazet, J., Husson, M.F., 2016. Package 'FactoMineR'. In: Obtenido de Multivariate Exploratory Data Analysis and Data Mining. http://cran/.r-project.org/web/packages/FactoMineR/FactoMineR.
Jouzel, J., Alley, R.B., Cuffey, K., Dansgaard, W., Grootes, P., Hoffmann, G., Johnsen, S.J., Koster, R., Peel, D., Shuman, C., 1997. Validity of the temperature reconstruction from water isotopes in ice cores. J. Geophys. Res.: Oceans 102 (C12), 26471–26487.
Kaufman, D., Ager, T., Anderson, N., Anderson, P., Andrews, J., Bartlein, P., Brubaker, L., Coats, L., Cwynar, L.C., Duvall, M., 2004. Holocene thermal maximum in the western Arctic (0-180°W). Quat. Sci. Rev. 23 (5–6), 529–560.
Kaufman, D.S., Schneider, D.P., McKay, N.P., Ammann, C.M., Bradley, R.S., Briffa, K.R., Lakes, A., 2009. Recent warming reverses long-term Arctic cooling. Science 325 (5945), 1236–1239.
Kylander, M.E., Ampel, L., Wohlfarth, B., Veres, D., 2011. High-resolution X-ray fluorescence core scanning analysis of Les Echets (France) sedimentary sequence: new insights from chemical proxies. J. Quat. Sci. 26 (1), 109–117.
Lapointe, F., Francus, P., Lamoureux, S.F., Saïd, M., Cuven, S., 2012. 1750 years of large rainfall events inferred from particle size at East Lake, Cape Bounty, Melville Island, Canada. J. Paleolimnol. 48 (1), 159–173.
Lapointe, F., Francus, P., Lamoureux, S.F., Vuille, M., Jenny, J.P., Bradley, R.S., Massa, C., 2017. Influence of North Pacific decadal variability on the western Canadian Arctic over the past 700 years. Clim. Past 13 (4), 411–420.
Lewis, T., Braun, C., Hardy, D.R., Francus, P., Bradley, R.S., 2005. An extreme sediment transfer event in a Canadian High Arctic stream. Arctic Antarct. Alpine Res. 37 (4), 477–482.
Lewkowicz, A.G., Hartshorn, J., 1998. Terrestrial record of rapid mass movements in the Sawtooth range, Ellesmere Island, northwest Territories, Canada. Can. J. Earth Sci. 35 (1), 55–64.
Madsen, A.T., Murray, A.S., 2009. Optically stimulated luminescence dating of young sediments: a review. Geomorph 109 (1), 3–16.
Major, J.J., 2003. Debris flow. In: Middleton, G.V. (Ed.), Encyclopedia of Sediments and Sedimentary Rocks. Kluwer, Dordrecht, pp. 186–188.
Masson-Delmotte, V., Landais, A., Stievenard, M., Cattani, O., Falourd, S., Jouzel, J., Johnsen, S.J., Dahl-Jensen, D., Sveinsbjornsdottir, A., White, J., 2005. Holocene climatic changes in Greenland: different deuterium excess signals at Greenland ice core project (GRIP) and north GRIP. J. Geophys. Res. Atmos. 110 (D14).
McWethy, D.B., Whitlock, C., Wilmshurst, J.M., McGlone, M.S., Fromont, M., Li, X., Dieffenbacher-Krall, A., Hobbs, W.O., Fritz, S.C., Cook, E.R., 2010. Rapid landscape transformation in South Island, New Zealand, following initial Polynesian settlement. Proc. Nati. Acad. Sci. U.S.A 107 (50), 21343–21348.
Mejdahl, V., Christiansen, H.H., 1994. Procedures used for luminescence dating of sediments. Quat. Sci. Rev. 13 (5–7), 403–406.
Mulder, T., Alexander, J., 2001. The physical character of subaqueous sedimentary density flows and their deposits. Sedimentology 48 (2), 269–299.
Murray, A.S., Olley, J.M., 2002. Precision and accuracy in the optically stimulated luminescence dating of sedimentary quartz: a status review. Geochronometria 21 (1), 1–16.
Murray, A.S., Wintle, A.G., 2003. The single aliquot regenerative dose protocol: potential for improvements in reliability. Radiat. Meas. 37 (4), 377–381.
Normandeau, A., Brown, O., Jarrett, K., Francus, P., De Coninck, A., 2019. Epoxy impregnation of unconsolidated marine sediment core subsamples for the preparation of thin sections at the Geological Survey of Canada (Atlantic). Geol. Surv. Canada. Technical Note 10, 10 p. https://doi.org/10.4095/313055.
Olley, J.M., De Deckker, P., Roberts, R.G., Fifield, L.K., Yoshida, H., Hancock, G., 2004. Optical dating of deep-sea sediments using single grains of quartz: a comparison with radiocarbon. Sediment. Geol. 169 (3), 175–189.
Perren, B.B., Bradley, R.S., Francus, P., 2003. Rapid lacustrine response to recent high arctic warming: a diatom record from Sawtooth Lake, Ellesmere Island. Nunavut. Arc. Antarc. Alp. Res. 35 (3), 271–278.
Prescott, J.R., Hutton, J.T., 1994. Cosmic ray contributions to dose rates for luminescence and ESR dating: large depths and long-term time variations. Radiat. Meas. 23 (2–3), 497–500.
R Development Core Team, 2008. R: A language and environment for statistical computing. R Foundation for Statistical Computing, Vienna, Austria. Available at: http://www.r-project.org/.
Scheffler, K., Buehmann, D., Schwark, L., 2006. Analysis of late Palaeozoic glacial to postglacial sedimentary successions in South Africa by geochemical proxies–response to climate evolution and sedimentary environment. Palaeogeogr. Palaeoclimatol. Palaeoecol. 240 (1), 184–203.
St-Onge, G., Mulder, T., Piper, D.J., Hillaire-Marcel, C., Stoner, J.S., 2004. Earthquake and flood-induced turbidites in the Saguenay Fjord (Québec): a Holocene paleoseismicity record. Quat. Sci. Rev. 23 (3), 283–294.
Valet, J.-P., Tanty, C., Carlut, J., 2017. Detrital magnetization of laboratory-redeposited sediments, Geophys. J. Intern. 210 (1), 34–41.
Vinther, B.M., Clausen, H.B., Fisher, D.A., Koerner, R.M., Johnsen, S.J., Andersen, K.K., Dahl-Jensen, D., Rasmussen, S.O., Steffensen, J.P., Svensson, A.M., 2008. Synchronizing ice cores from the Renland and Agassiz ice caps to the Greenland ice core chronology. J. Geophys. Res. D Atmos. 113 (8).
Wintle, A.G., Murray, S.A., 2006. A review of quartz optically stimulated luminescence characteristics and their relevance in single-aliquot regeneration dating protocols. Radiation Meas. 41 (4), 369–391.
Xuan, C., Channell, J.E., 2009. UPmag: MATLAB software for viewing and processing u channel or other pass-through paleomagnetic data. Geochem. Geophys. Geosyst. 10 (10).
Zolitschka, B., Francus, P., Ojala, A.E., Schimmelmann, A., 2015. Varves in lake sediments–a review. Quat. Sci. Rev. 117, 1–41.